IMMUNOLOGY

The chaperonin CCT controls T cell receptor–driven 3D configuration of centrioles

N. B. Martin-Cofreces[1,2,3]*[†], F. J. Chichon[4][†], E. Calvo[3,5], D. Torralba[1,2], E. Bustos-Moran[1,2],
S. G. Dosil[1,2], A. Rojas-Gomez[1,2], E. Bonzon-Kulichenko[3,5], J. A. Lopez[5], J. Otón[6], A. Sorrentino[7],
J. C. Zabala[8], I. Vernos[9,10,11], J. Vazquez[3,5], J. M. Valpuesta[4]*[‡], F. Sanchez-Madrid[1,2,3]*[‡]

T lymphocyte activation requires the formation of immune synapses (IS) with antigen-presenting cells. The dynamics of membrane receptors, signaling scaffolds, microfilaments, and microtubules at the IS determine the potency of T cell activation and subsequent immune response. Here, we show that the cytosolic chaperonin CCT (chaperonin-containing TCP1) controls the changes in reciprocal orientation of the centrioles and polarization of the tubulin dynamics induced by T cell receptor in T lymphocytes forming an IS. CCT also controls the mitochondrial ultra-structure and the metabolic status of T cells, regulating the de novo synthesis of tubulin as well as posttranslational modifications (poly-glutamylation, acetylation, Δ1 and Δ2) of αβ-tubulin heterodimers, fine-tuning tubulin dynamics. These changes ultimately determine the function and organization of the centrioles, as shown by three-dimensional reconstruction of resting and stimulated primary T cells using cryo–soft x-ray tomography. Through this mechanism, CCT governs T cell activation and polarity.

INTRODUCTION

The centrosome is a nonmembranous organelle in charge of organizing the microtubule (MT) network, maintaining the global organization of cellular organelles and intracellular transport between different organelles during interphase in eukaryotic cells from animal origin. It is formed by two barrel-shaped structures called centrioles, surrounded by an amorphous material, called the pericentriolar matrix (PCM) (1). The centrosome has been shown to play an active role during immune synapse (IS) formation, helping sustained activation in CD4 T cells (2) and guiding the polarized translocation of the intracellular secretory machinery and organelles toward the contact area with the antigen-presenting cell (APC) in CD4 and CD8 T cells for specific cell-cell communication (3–5). Centrosome positioning at the IS is considered a hallmark for T cell activation (6).

Local redistribution of specific plasma membrane receptors and cytosolic protein clusters is observed during IS formation (7), which is associated with cytoskeletal reorganization (8, 9). Mitochondria are the organelles that control cellular metabolism, and during T cell activation, they undergo changes in their shape and localization, which determine their ability to produce adenosine 5′-triphosphate

(ATP). This is reflected by changes in the mitochondrial membrane potential, influencing the proton gradient across the membrane. The movement of mitochondria toward the IS has been previously reported; drp-1 (dynamin-related protein 1) is needed to reduce their size for proper accumulation at the IS along MTs to aid T cell activation (10). Localization of mitochondria at the IS provides control of local calcium (11) and ATP levels (10).

Despite its prominent role in T cell activation, the molecular mechanisms controlling centrosome-related proteostasis (including protein synthesis, transport into and out of the centrosome area, and degradation) and internal organization at the IS are mostly unknown. Through Systems Biology analysis, we identified the increase in cytosolic CCT chaperonin in centrosome fractions from IS-forming T lymphocytes. Proteins must undergo complex folding processes to be fully functional, and a number of proteins require the help of molecular chaperones to acquire their correct three-dimensional (3D) structure. The eukaryotic cytosolic chaperonin-containing TCP1 [CCT; also called TRiC (TCP1 ring complex)] is a large macromolecular complex (~1 MDa) made up of two copies of eight homologous subunits that assemble to form a double-ring structure (12–14). The 3D ultrastructure of activated, polarized T cells by cryo–soft x-ray tomography (cryo-SXT), stimulated emission depletion (STED) confocal microscopy, and live cell total internal reflection fluorescence microscopy (TIRFm) showed that interfering with CCT expression prevents correct centriolar and mitochondrial ultrastructure and localization. Our findings link the de novo synthesis of tubulin and MT dynamics through CCT function, which ultimately regulate cell polarity.

RESULTS

T cell receptor–driven changes in pericentriolar proteome composition

To address possible coordinated changes in protein complexes at the centrosome area during T cell activation, we first compared using quantitative mass spectrometry–based proteomics: isobaric tags for relative and absolute quantitation (iTRAQ), centrosome-enriched

[1]Immunology Service, Hospital Universitario de la Princesa, UAM, IIS-IP. Madrid, 28006 Spain. [2]Area of Vascular Pathophysiology, Laboratory of Intercellular Communication, Fundación Centro Nacional de Investigaciones Cardiovasculares-Carlos III, Madrid, 28029 Spain. [3]Centro de Investigación Biomédica en Red de Enfermedades Cardiovasculares (CIBERCV), 28029 Spain. [4]Department of Macromolecular Structure, Computational Systems Biology Group, Centro Nacional de Biotecnología (CNB-CSIC), Madrid, 28049, Spain. [5]Laboratory of Cardiovascular Proteomics. Fundación Centro Nacional de Investigaciones Cardiovasculares-Carlos III, Madrid, 28029 Spain. [6]Structural Studies Division, MRC Laboratory of Molecular Biology, Francis Crick Avenue, Cambridge CB2 0QH, UK. [7]ALBA Synchrotron Light Source, Cerdanyola del Vallès, Barcelona 08290, Spain. [8]Departament of Molecular Biology, Facultad de Medicina, Universidad de Cantabria, Santander, 39005 Spain. [9]Centre for Genomic Regulation (CRG), The Barcelona Institute of Science and Technology, Dr Aiguader 88, Barcelona, 08003, Spain. [10]Universitat Pompeu Fabra (UPF), Dr Aiguader 88, Barcelona 08003, Spain. [11]ICREA, Pg. Lluis Companys 23, Barcelona 08010, Spain.
*Corresponding author. Email: fsmadrid@salud.madrid.org (F.S.-M.); jmv@cnb.csic.es (J.M.V.); noa.martin@salud.madrid.org (N.B.M.-C.)
†These authors contributed equally to this work.
‡These authors contributed equally to this work.

fractions from CD3ε/CD28-activated and resting human primary T lymphocytes (as depicted in Fig. 1A and fig. S1A), to discover clusters of proteins whose amount change upon activation at the centrosomal region. We used an approach based on cold to stop activation and initiated centrosome isolation (15) avoiding cytoskeleton-disrupting drugs such as nocodazole or cytochalasin D, which are known to impair T cell activation (8). The steps for biochemical isolation are depicted in fig. S1A (15, 16). We confirmed that activated centrosomes were able to increase in vitro polymerization of tubulin when used as lattices (Fig. 1B), suggesting a centrosome maturation process upon T cell receptor (TCR) activation. CCT was highly enriched in the centrosome area upon T cell activation. CCT participates in the folding of a number of substrates such as tubulin and actin and constitutes a nonpromiscuous chaperonin compared to other known chaperones (17). CCT allows αβ-tubulin heterodimers to form for further incorporation into MTs, helped by tubulin cofactors (TBCs) (18). Quantitative data from six biological replicates were subjected to statistical and systems analysis using the Systems Biology Triangle (SBT) model to detect coordinated protein responses (Fig. 1, C and D; fig. S1B; and tables S1 and S2) (19).

The coordinated increases in some protein groups were consistent with already known events in T cell stimulation, whereas others corresponded to unknown changes. These include (i) tubulins, which support tubulin polymerization from the centrosome at the IS; (ii) the human leukocyte antigen complex and different components of CXCR4, known to be involved in T cell activation; (iii) heterogeneous nuclear ribonucleoproteins; (iv) the CCT chaperone; (v) Hsp90 chaperones and the cdc34 co-chaperone, which help CCT in the folding of different clients; and (vi) the proteasome. These data suggest that the activated centrosomal region most likely acts as a specific site for regulation of protein folding and degradation. Conversely, there was a coordinated decrease of (i) T cell signaling components; (ii) the Rich/Amot polarity complex, involved in organization of apical-polarity proteins; (iii) the p-SLP-76 ADAP-Ena–Vasodilator-stimulating protein (VASP) complex, implicated in costimulation of T cells; (iv) the WASP-interacting protein, Wiskott-Aldrich syndrome protein and myosin IIa (WIP-WASP-myosin IIa) complex, participating in IS formation in natural killer cells; and (v) some cytoskeletal proteins (septins and dynamins), ribosomes, DNA repair, and chromosome structural proteins. An additional functional network analysis using Cytoscape revealed that the majority of altered proteins formed part of dense protein clusters displaying organized expression changes (Fig. 1E and fig. S1C).

One of these clusters contained α- and β-tubulin and tubulin-related components, as well as β-actin (Fig. 1E), in agreement with the SBT results. Both SBT and network analysis indicated a clear up-regulation of the eight subunits of the cytosolic chaperonin CCT complex. CCT changes in all the replicates are depicted in the bottom graph of Fig. 1C. In this CCT-related cluster, β-actin and several isoforms of α and β tubulins were increased. The tubulin-binding cofactor B (TBCB), which helps CCT to maintain tubulin in its correctly folded conformation (17), also increased in the activated centrosomal fractions (Fig. 1D). CCT enrichment in fractions corresponding to centrosomes from activated T cells was also biochemically corroborated (Fig. 1F). These centrosome modifications were also studied in samples from Jurkat lymphoblastoid T cells isolated through a more stringent method using nocodazole and cytochalasin D treatment (see fig. S1A) (16). The corresponding centrosomal fractions were subjected to tubulin polymerization assays in *Xenopus laevis* egg extracts, showing similar behavior to primary T lymphoblasts (fig. S2A). Selected fractions were analyzed for protein content by

label-free proteomics, which confirmed the enrichment upon activation of the eight subunits of the CCT complex (fig. S2B and table S3).

CCT localizes at the IS in antigen-driven T-APC contacts (Fig. 1G). To assess the role of CCT in the reorganization of the tubulin-based cytoskeleton, critical for proper IS formation (20), we simultaneously knocked down (KD) four of the eight CCT subunits [siRNAs specific for the CCT subunits CCT1, CCT2, CCT4, and CCT5 (siCCT); and control siRNA (siCtrl) for cells treated with control small interfering RNAs (siRNAs); fig. S3A], specifically those involved in direct contact with tubulin and actin during their folding (21) and in ATP consumption (22). We studied MT growth by TIRFm, which strictly allows visualization of the IS plane, closely apposed to the cover glass (Fig. 1, H and I, and movie S1). EB3 (end-binding 3) protein binds to the MT plus ends, and its forward and backward movements indicate MT growth or shrinking modes, respectively (23). The number of tracks emerging from the centrosome area was reduced in siCCT-treated cells, as well as the growing speed and displacement of the EB3-enriched tips (Fig. 1, H and I).

CCT regulates tubulin dynamics and posttranslational modifications at the IS

To determine the mechanism involving CCT activity in the control of MT polymerization during IS formation for proper T cell activation, we analyzed the availability of αβ-tubulin and their posttranslational modifications (PTMs) induced by stimulation of the TCR, using native immunoelectrophoresis and specific antibodies against total and modified tubulins. Analysis of soluble, native αβ-tubulin showed that available heterodimers increased upon activation and that CCT silencing induced their accumulation in both resting and activating conditions (Fig. 2A), despite the fact that depletion of CCT subunits did not cause any change in global actin and tubulin content, as observed by Western blot (fig. S3A). No clear defects in the MT organization in resting cells were detected by immunofluorescence (fig. S3B). Tubulin subunits undergo common and distinct PTMs upon MT polymerization and depolymerization, which determine MT stability and their ability to bind different partners such as MT-associated proteins (MAPs) or molecular motors that move cargos along them (24). One of these PTMs is detyrosination of α-tubulin C-terminal EEY into EE [resulting from detyrosination by cytosolic carboxypeptidases; Δ1-α-tubulin], which increases upon TCR activation and helps rapid depolymerization due to kinesin 13 binding (25). The content of Δ1-α-tubulin in soluble heterodimers markedly decreased in siCCT cells (Fig. 2B). Together with decreased speed of EB3–green fluorescent protein (GFP)–decorated plus tips (Fig. 1, H and I), this indicated that heterodimers in siCCT cells were not incorporated into MTs long enough to undergo PTMs. Moreover, removal of the tyrosine and glutamic acid C-terminal residues (forming Δ2-α-tubulin) paralleled the kinetics of glu-α-tubulin increase upon TCR activation in siCtrl cells but not in siCCT cells (Fig. 2C). We also performed these analyses in T cell total lysates under denaturing conditions, which do not discriminate between soluble and insoluble tubulins (fig. S3C).

To assess the consequences of the decrease in tubulin polymerization on the organization of the MT network, we analyzed polyglutamylation (pE) of αβ-tubulin, which indicates stabilization of polymerized MTs and which increased in siCtrl cells upon activation (Fig. 2D). The siCCT cells showed higher pE–αβ-tubulin under resting conditions, pointing to the presence of highly stabilized MTs before TCR stimulation. In addition, acetylation of α-tubulin at K40, a landmark for MT stabilization, resulted in a similar kinetic to pE
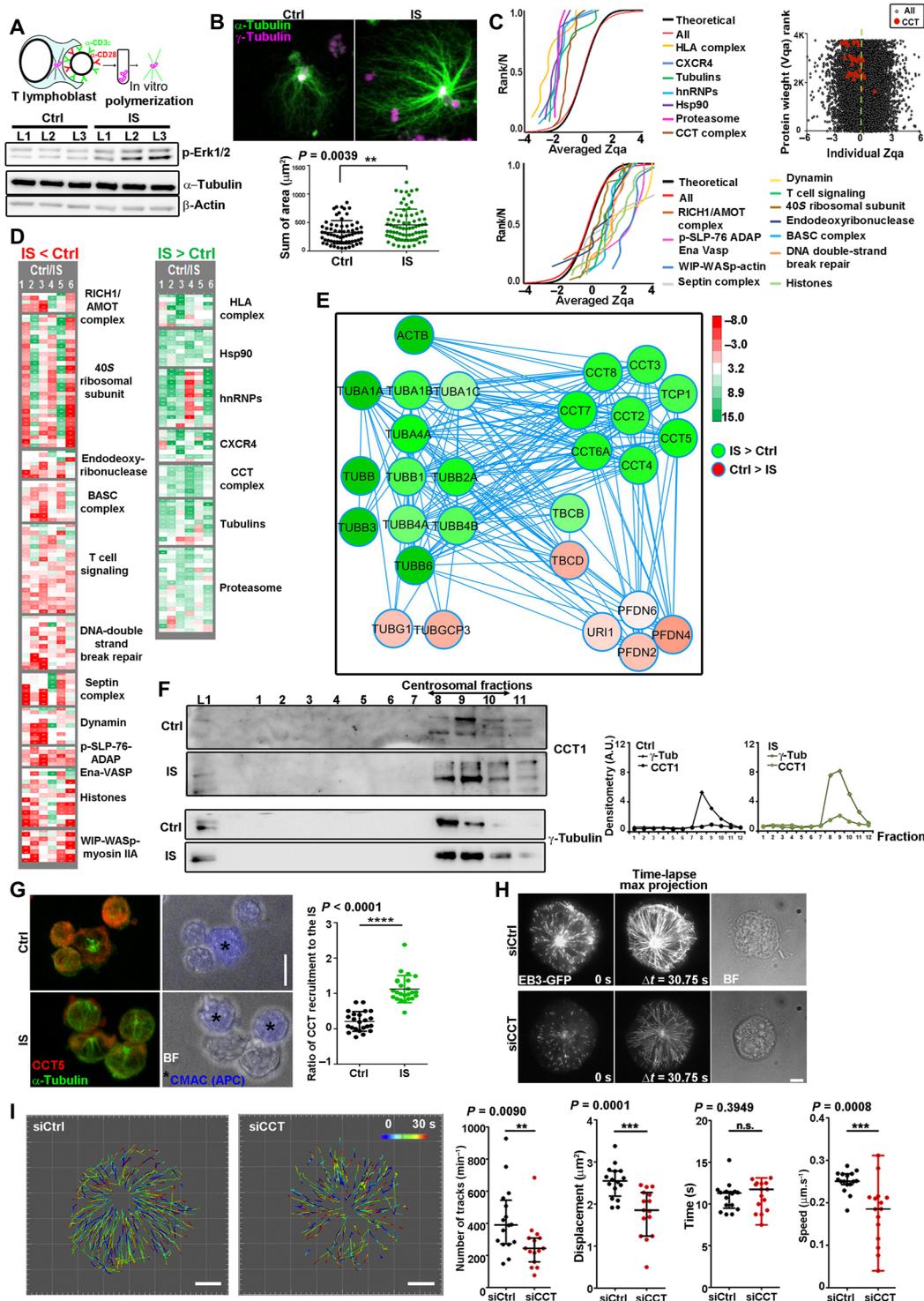
Fig. 1. Pericentriolar Systems Biology regulation upon polarized T cell receptor and CD28 activation. (**A**) Workflow for IS formation, centrosome-enriched fraction isolation and in vitro polymerization assay, Western blot, and Erk1/2 activation. (**B**) Fluorescence from rhodamine–α-tubulin and γ-tubulin. Graph, rhodamine–α-tubulin in MTs (Ctrl, $n = 66$; IS, $n = 76$; Mann-Whitney). (**C**) iTRAQ (six replicates, 30 donors). Left graphs: Coordinated protein alterations in functional categories at centrosomes during IS. Zqa' values, standardized log$_2$ ratio averages of proteins (stimulated versus control). Right: Global distribution of the eight CCT subunits. Zq < 0, CCTs versus other proteins. BASC, super complex of BRCA1-associated proteins. (**D**) Systems Biology analysis of the six biological replicates showing coordinated increases/decreases. The SBT algorithm was applied. (**E**) Cytoscape map from the SBT analysis. (**F**) Western blot, centrosome-enriched fractions processed in (B) to (E). Graph, densitometric analysis. (**G**) CCT5 subunit localization in conjugates with APCs (*Raji cells). Scale bars, 10 μm. Graph, CCT5 at the IS (means ± SEM, Ctrl $n = 23$, IS $n = 24$; Mann-Whitney). (**H** and **I**) MT dynamics in activated Jurkat cells by TIRFm. (H) Fluorescence images, start point, and maximal projection of the time lapses (Δt); BF, bright field. Scale bar, 5 μm. (I) Imaris-generated track maps. Scale bars, 5 μm. Graphs, statistics for tracks (median ± interquartile range; $n = 15$; Mann-Whitney). A.U., arbitrary units; n.s., not significant. *$P < 0.05$, **$P < 0.01$, ***$P < 0.001$.
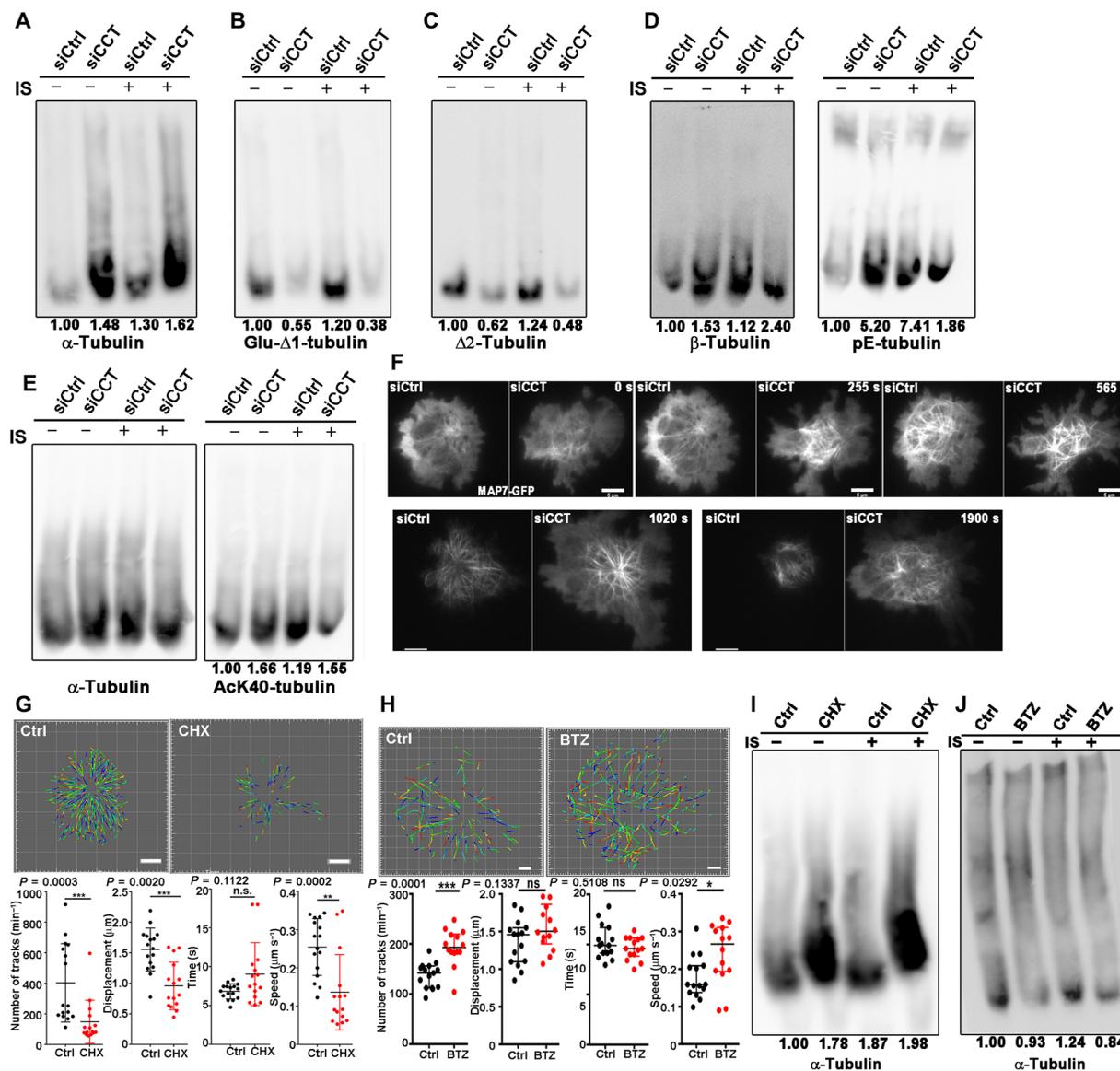
Fig. 2. CCT regulates tubulin dynamics at the IS. (**A** to **C**) Native immunoelectrophoresis of αβ-tubulin complexes in resting and activated siCtrl or siCCT Jurkat T cells detected with anti–α-tubulin (A) and PTMs for Δ1-α-tubulin (B) and Δ2-α-tubulin (C). (**D** and **E**) Native immunoelectrophoresis against total α-tubulin (E) and β-tubulin (D) antibodies, pE-tubulin (D), and acetylated K40 α-tubulin (E). $n = 3$. (**F**) Analysis of MT dynamics in activated Jurkat T cells cotransfected with MAP7-GFP and siCtrl or siCCT by TIRFm; $n = 3$. Scale bars, 5 μm. (**G**) Cells transfected with EB3-RFP were treated or not with cycloheximide (CHX) for 40 min and allowed to spread over a stimulating surface before TIRFm analysis. Imaris track analysis is shown (15 s; $n = 16$, siCtrl and CHX; Mann-Whitney). (**H**) Cells stably expressing low amounts of EB3-GFP were treated or not with bortezomib (BTZ; 520 nM) for 2 hours and allowed to spread over a stimulating surface before TIRFm analysis. Imaris track analysis is shown (30 s; Ctrl $n = 15$, BTZ $n = 14$; Mann-Whitney). (**I** and **J**) Native immunoelectrophoresis of αβ-tubulin complexes in resting and activated T cells treated with CHX (I) or BTZ (J) detected with anti–α-tubulin. $n = 3$, at least. Numbers correspond to normalized (Ctrl) densitometry analysis (Image Gauge software). *$P < 0.05$, **$P < 0.01$, ***$P < 0.001$.

after stimulation (Fig. 2E). These results correlated with the lack of reorganization of the tubulin cytoskeleton at the IS, as observed using MAP7-GFP, a MAP that binds to and stabilizes MTs. Accordingly, the organization in siCCT cells of MTs at the IS initially appeared disordered, with a clear delay in the centrosome-dependent, radial distribution seen in siCtrl cells, as suggested by MAP7-GFP TIRFm imaging during IS formation (Fig. 2F and movie S2). Therefore, CCT regulates the dynamics of the tubulin network and reduces the growth of MTs, thereby inducing a more stabilized MT network.

These data suggest that the processes of synthesis, folding, polymerization, and degradation of tubulins are interconnected in T cells and is promoted by TCR activation. CCT activity is needed for tubulin folding after its synthesis (26). To ascertain whether the synthesis or degradation of proteins affect tubulin polymerization, we assayed the effect of lack of synthesis by a short cycloheximide (CHX) treatment (20 μg/ml for 40 min) and lack of degradation by bortezomib (BTZ) treatment (an inhibitor of the proteasome). We observed a defective incorporation of heterodimers into MTs during T cell activation

with CHX, whereas BTZ increased polymerization, as observed by EB3 tracking using TIRFm (Fig. 2, G and H, and movies S3 and S4). We used low-expressing EB3 cells to assess the BTZ effect. The content in native αβ-tubulin increased with CHX treatment (Fig. 2I) but was reduced with BTZ (Fig. 2J), which supports the notion that tubulin dynamics is regulated by synthesis and degradation balance.

3D cellular ultrastructure depends on CCT polarized activity

To address the mechanistic role of CCT in IS formation, we imaged resting and stimulated human primary CD4 T cells using cryo-SXT, which allows direct visualization of thick specimens (up to 10 μm) upon vitrification and their 3D reconstruction in the 50-nm resolution range (27). Primary CD4 T cells from healthy donors were treated with control siRNA (siCtrl) or siRNA specific for the CCT subunits (siCCT), cotransfected with EB3-GFP and stained for MitoTracker Orange upon sorting for GFP for correlative cryo-microscopy (silencing is shown in fig. S4A and movies S5 to S8). The 3D reconstruction of whole cells allowed us to locate, through calculation of different parameters, the position of centrioles within the centrosome and with respect to the adhering surface (Figs. 3 and 4, A and B, and fig. S4B). First, the area of influence of the centrosome (AIC), which shows a different appearance from the rest of the cytoplasm and includes the PCM, the adjacent Golgi cisternae and the associated vesicular network, was assessed as a unique entity. The median AIC volume showed a tendency to increase upon stimulation in siCtrl cells (Fig. 4B). TCR activation did not affect centriole size, without apparent change in length (L) or radius (r); the distance (d) between the centers of the centrioles remained basically invariant (fig. S4B). Activation of TCR induced a decreased angle (a) between the centrioles in siCtrl cells but not in siCCT cells (from around 68° to around 29° in siCtrl cells; Fig. 4C). The centriole pair in siCtrl cells showed a tendency to adopt a parallel orientation with respect to the plane of the IS, which changed markedly upon activation, although CCT KD reverted this change (angle α, Fig. 4D). Both siCtrl and siCCT centrosomes showed little or no change in their coplanar distribution upon stimulation (angle A, Fig. 4E). The centrosome polarized at the IS upon TCR activation in the majority of cells analyzed [about 70 to 80% either in mouse or human cells; (2, 4)]. However, part of them was not located at the IS. We observed that the EB3-decorated tracks emerging from the centrosome are directed toward the IS, although the centrosome is not near the IS (Fig. 4F and movie S9). We propose that the specific disposition of the centrioles inside the centrosome and the orientation of the centriole pair with respect to the IS are responsible for this effect (Fig. 4G). The MT stabilization induced by CCT KD probably prevents the changes induced in the centriole pair by TCR activation in siCCT cells. This may also affect the arrangement of the mitochondrial network, which does not change its average volume (fig. S4C), although mitochondria undergo changes in their individual radius. The mitochondria of siCCT cells show a decreased radius, which increases with activation, whereas the control cells show a tendency to reduce their radius upon 15 min of activation (fig. S4D). Cell viability was not affected by siCCT KD (fig. S4E).

CCT KD prevents correct centrosomal orientation, which is also observed for the Golgi apparatus (GA). In siCtrl cells, the GA organized around the centrosome and was localized near the IS, as imaged by STED microscopy. siCCT cells also showed the GA around the centrosome, but it was partially polarized and displayed a different orientation of the cisternae (fig. S5, A to C). In contrast, T cell actin–based frontal lamella contacting the APC seemed unaffected

by CCT depletion, as observed by STED microscopy (fig. S5, B and C). Moreover, phosphorylation of the myosin light chain was not affected by siCCT upon TCR activation (fig. S5D).

CCT regulates signaling at the IS and nanovesicle dynamics

The intracellular traffic at the IS sustains TCR signaling and requires a correct centrosome function (2, 20). We observed a decreased signaling in siCCT cells, as determined by reduced phosphorylation of CD3ζ (Y83), LAT (Y132), and PLCγ1 (Y783) (Fig. 5A). We also studied Nuclear factor for activated T cells (NFAT) dephosphorylation in response to the TCR-dependent increase in calcium flow, which was reduced in siCCT cells (Fig. 5B). Nuclear factor κB (NFκB) phosphorylation showed a tendency to decrease in siCCT cells, pointing to defects in these signaling pathways. To ascertain the organization of TCR/CD3 complexes at the IS surface, we assessed CD3ε clustering through confocal microscopy. siCCT cells were less efficient in forming the CD3ε central cluster (Fig. 5C). However, this effect was not due to defective surface expression of CD3ε in the T cells, as assessed by flow cytometry (Fig. 5D). We therefore analyzed the nanovesicle trafficking beneath the plasma membrane at the IS, to ascertain its possible contribution to this defect. Jurkat cells cotransfected with both EB3-GFP and CD3ζ-mCherry along with siCCT showed a reduction in the number and speed of CD3ζ-bearing vesicles (albeit with increased duration). Their trajectories followed a more peripheral circuit rather than localizing at the center of the IS (Fig. 5E and movie S10), therefore suggesting a defect in their contribution to signaling at the IS as repositories of signaling molecules and/or by directly spreading the TCR/CD3 signaling (20).

CCT regulates mitochondrial positioning and function

Since mitochondria are known to polarize toward the IS in an MT-dependent manner and to sustain local calcium increases (10, 11), we assessed their localization and function. siCCT cells also showed defects in normal mitochondria polarization and fragmentation at the IS, as illustrated by MAP7-GFP relative localization under TIRFm (Fig. 6A and movies S11 and S12). STED imaging of whole cells confirmed these results (Fig. 6B and movies S13 and S14), corresponding to a defective movement if mitochondrial fission is defective (10). The mitochondrial mass was not affected (Fig. 6C and fig. S6, A and B). This is in accordance with a lack of response of mitochondria in terms of membrane depolarization (Fig. 6D) and a concomitant decrease in ATP production upon activation (measured fold induction of 1.514 ± 0.069 in siCtrl versus 1.399 ± 0.102 in siCCT, means ± SEM; Fig. 6E). The basal mitochondrial respiration of siCCT cells was similar to control cells, whereas the increase in respiration [oxygen consumption rate (OCR)] observed upon T cell activation was lower in siCCT cells, as was their maximal respiration rate (Fig. 6F and table S4). Also, the extracellular acidification rate (ECAR), an indicator of glycolysis, was similar under basal conditions for siCtrl and siCCT cells and showed a parallel decrease in activated siCCT cells (Fig. 6F). The analysis of the mean fluorescence intensity of living T cells TIRFm also revealed that mitochondria were less active at the IS in siCCT cells (Fig. 6G and movie S15). Video microscopy imaging of Jurkat-Raji conjugates showed that CCT silencing caused mislocalization of mitochondria from the IS area (Fig. 6H and movies S16 and S17). These data support the role of CCT in regulating T cell metabolism during T cell activation.

Mamalian Target of rapamycin complex 1 (mTORC1)–associated signaling, a marker for immune metabolic status, was defective in
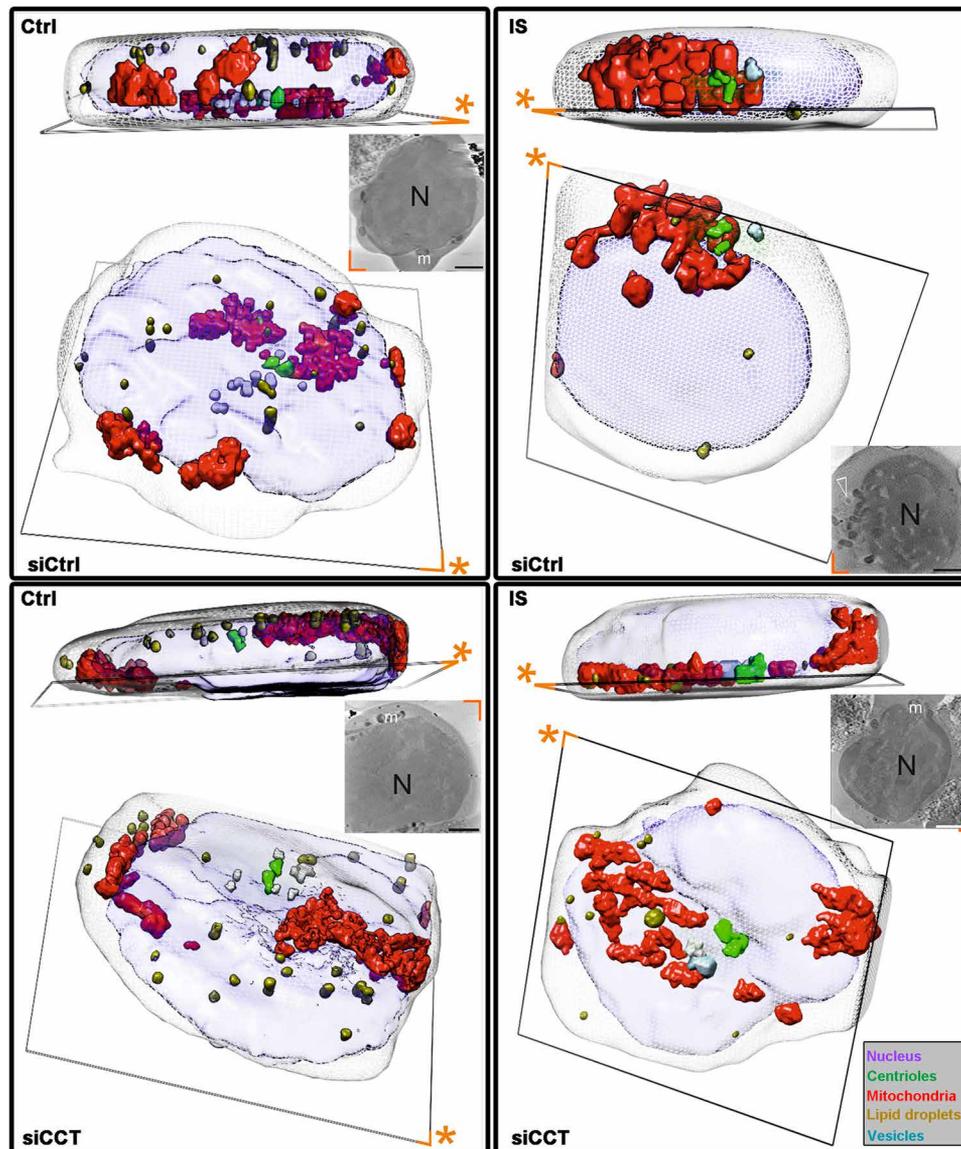
Fig. 3. CCT regulates the 3D T cell organization at synaptic contacts. 3D reconstructions of cryo-SXT images showing resting (Ctrl) and IS-forming (IS) human primary CD4 T cells, treated with control siRNA (siCtrl) or siRNAs for CCT (siCCT). Blue, nucleus; transparent grid, plasma membrane; red, mitochondria; green, centrioles; white, vesicles; olive, lipid droplets (colors may change due to superposition of the nucleus). Asterisks indicate same corner for the two views. Insets: Slices of the reconstructed cryo-SXT imaging. N, nucleus; m, mitochondria. Scale bars, 500 nm. The size of the squares indicating the carbon surface is 5 μm.

siCCT cells, accompanied by a decreased phosphorylation of the S6 ribosomal subunit in human primary CD4 T cells (Fig. 6I and fig. S6A) and in Jurkat T cells (fig. S6C), which supports a decrease in protein synthesis. Recent evidence has shown that CCT assists LS8 and Raptor (Regulatory-associated protein of TOR) folding, two subunits of the mTOR complex, therefore forming a feedback loop between TCR activation, protein synthesis, and tubulin dynamics (*28*). On the other hand, the mTOR complex is known to associate to the lysosomes upon activation (*29*); we therefore analyzed the localization of lysosome-associated membrane protein 1 (LAMP1)–positive vesicles in siCCT cells during IS formation, finding a defect in their accumulation around the centrosome upon TCR-dependent polarization (Fig. 6J). Interleukin-2 (IL-2) production, a late activation marker needed for T cell proliferation, decreased in siCCT cells stimulated by *Staphylococcus* enterotoxin-E

(SEE)–pulsed APCs (Fig. 6K). Cells silenced for individual CCT subunits showed a similar decrease in IL-2 secretion (fig. S6, D and E). In contrast, CD69 surface expression, an early activation marker, was similar in both siCtrl and siCCT cells (fig. S6, F and G), suggesting that cells sense the activation through the TCR although incompletely. These data indicate that upon polarizing stimulus, CCT is required to control the 3D orientation of centrioles and to organize correct MT growth and organization, facilitating changes in the centrosome that will allow correct cell polarity and activation.

DISCUSSION

Our data provide experimental evidence about the important role of the cytosolic chaperonin CCT in dynamic centriolar maturation
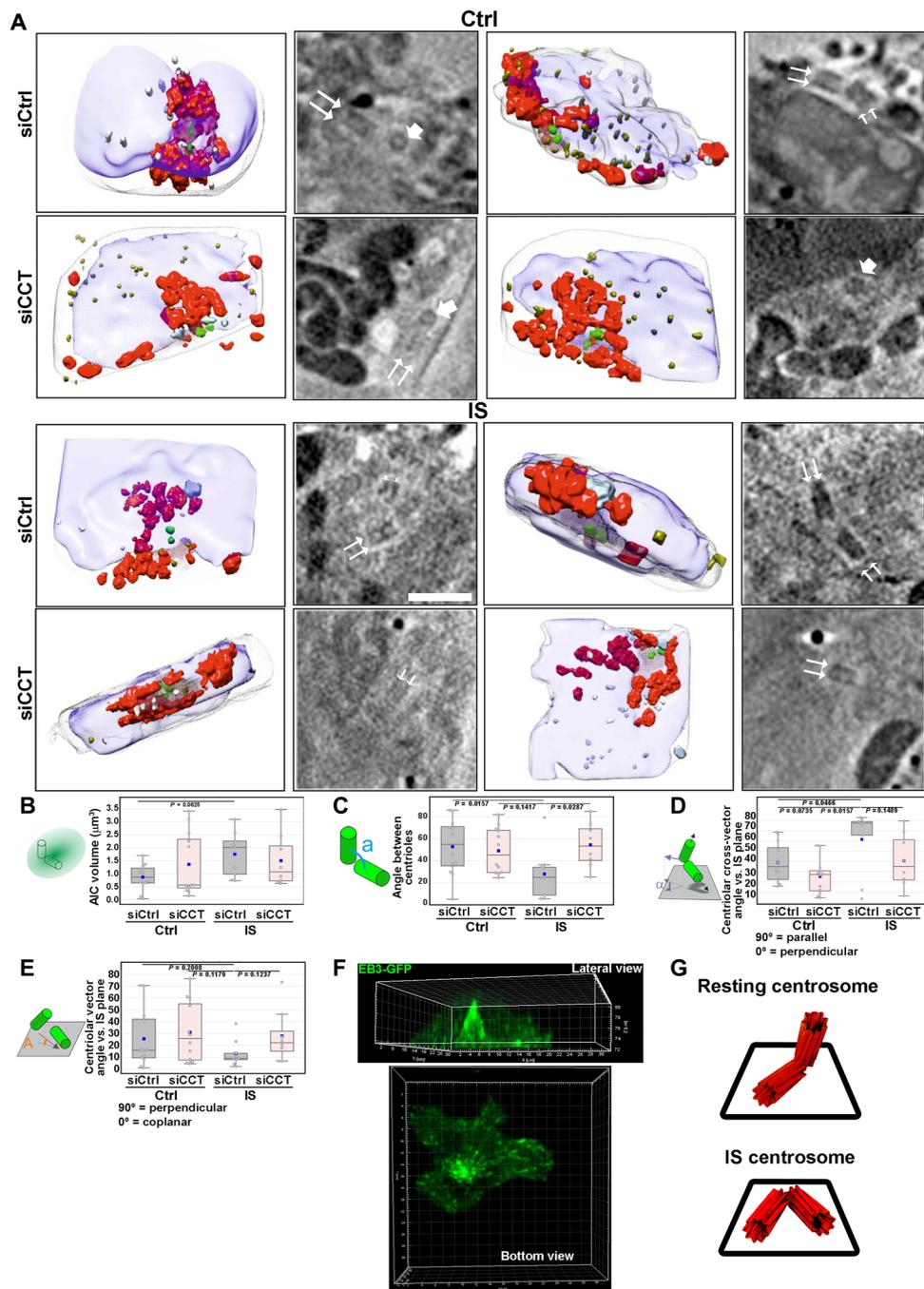
Fig. 4. CCT regulates the 3D centriolar organization at synaptic contacts. (**A**) Gallery of CD4 T cells 3D reconstructed after cryo-SXT. Mitochondria are shown in red, centrioles in green, vesicles in white, and lipid droplets in yellow. The right images correspond to a section of the area of AIC, including the centrioles (thin arrows: longitudinal section and wide arrows, cross section). Scale bar, 500 nm. (**B**) Volume of the AIC. (**C**) Centrosome internal angle (a). (**D**) Angle (A) between the vector joining the center of mass of each centriole and the IS plane. (**E**) Angle (α) between the centriolar cross-vector and the IS plane. Graphs, median and interquartile range. Blue dots, mean (n = 12, control siCtrl; n = 12, control siCCT; n = 9 IS siCtrl; n = 8, IS siCCT). (**F**) Resonant scanner confocal videomicroscopy of whole cells showing growing MT tips toward the IS. (**G**) Model for centriolar and centrosomal disposition respect to the IS plane in resting (Ctrl) and TCR-stimulated T cells (IS).

and cell polarization upon TCR activation and costimulation through CD28. We propose a mechanism involving the "de novo" synthesis of tubulin to sustain MT dynamics early upon T cell activation. This synthesis requires the correct folding of tubulin, which is assisted by CCT and maintained by tubulin-binding cofactors.

Here, we have used deep quantitative proteomics and Systems Biology to study the changes in human primary T cell centrosome composition that occur after stimulation and IS formation, avoiding pretreatment of cells with drugs targeting the cytoskeleton before TCR stimulation (15, 16, 30) to favor full T cell activation (8). In our
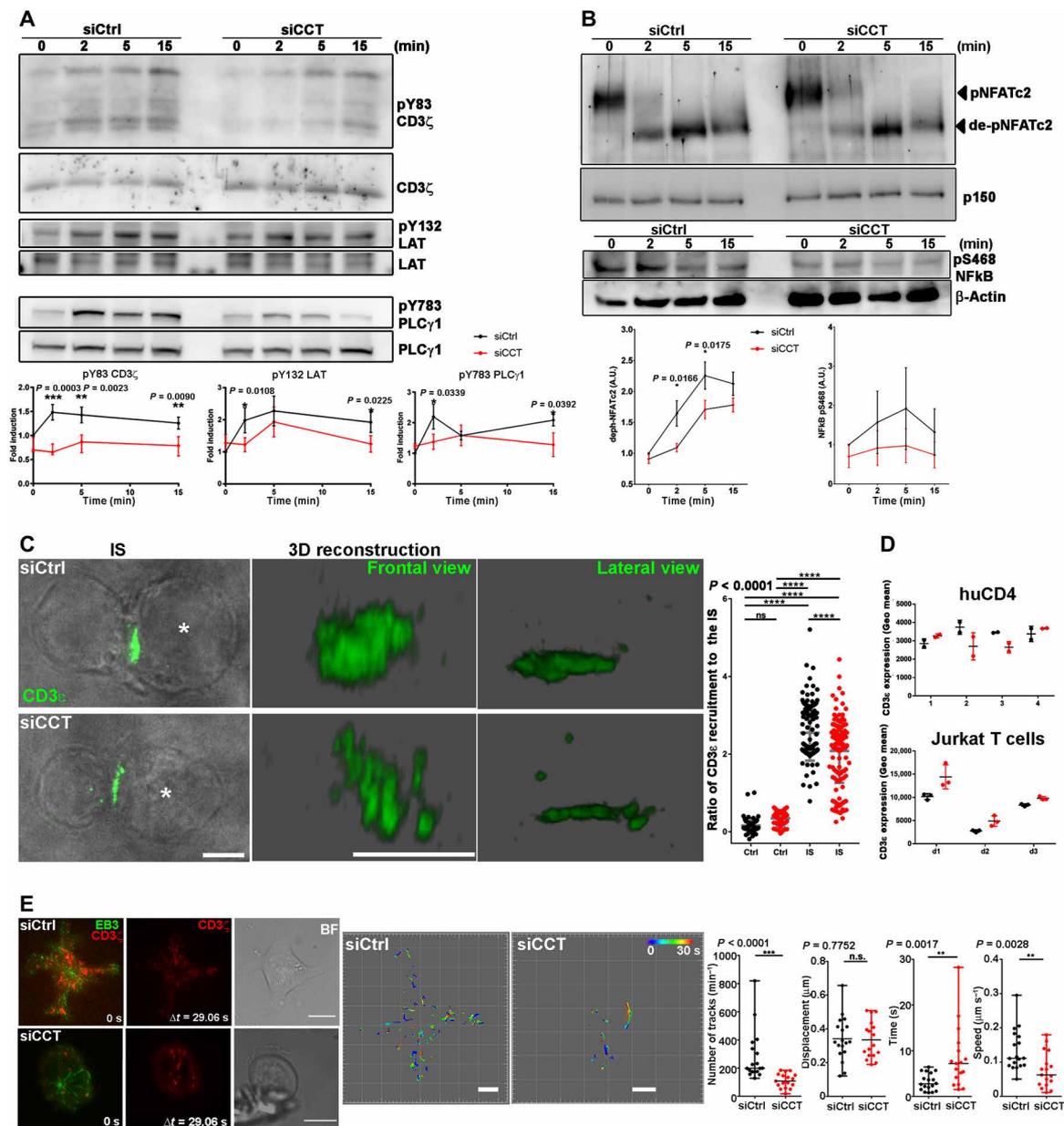
Fig. 5. CCT regulation of tubulin dynamics is required for TCR signaling and IS formation. (**A**) TCR downstream signaling of siCtrl- and siCCT-treated Jurkat T cells during activation: pY83-CD3ζ, pY132-LAT and pY783-PLCγ1. Total proteins, loading controls. Graphs, means ± SEM; n = 5. Two-way ANOVA. (**B**) NFATc2 and pS468-NFκB in primary human CD4 T cells. Graphs, means ± SEM. n = 3 and 4. One-way ANOVA. (**C**) CD3ε distribution at the IS in Jurkat T cells during synapse; a maximal projection of CD3ε is shown, merged with bright-field (BF) image; 3D reconstruction was performed with Leica LASX. Scale bar, 5 μm. Graph, CD3ε ratio at the IS by "synapse measures" algorithm. Mean and SD. One-way ANOVA [n = 63 (siCtrl Ctrl), 47 (siCCT Ctrl), 127 (siCtrl IS), and 156 (siCCT IS) from three independent experiments]. (**D**) CD3ε surface expression in human primary CD4 and Jurkat T cells (n = 4 and 3, respectively). (**E**) CD3ζ-bearing vesicle dynamics in activated T cells by TIRFm as in Fig. 1 (H and I). Scale bars, 10 μm. Imaris track maps and statistical analysis are shown (30 s; median plus interquartile range; Mann-Whitney test; n = 30). Scale bars, 5 μm. **P < 0.01; *P < 0.05.

experimental settings, the timing of activation corresponded to early T cell activation, concomitant with cytoskeleton remodeling and centrosome translocation toward the IS (15 to 20 min). At this stage, intracellular transport based on MT-dependent vesicular traffic to and from the IS is already established (9, 31). We observed upon T cell activation a coordinated increase of CCT, Hsp90 and its co-chaperone Cdc34, a number of tubulin α and β isoforms, actin and TBCB in the centrosome-enriched fractions. We therefore analyzed the role of CCT in T cell

activation. Mutations in isolated CCT subunits have implications for cell growth and gene expression, with different effects among different subunits in yeast (32). To avoid complications, we simultaneously silenced four of the eight CCT subunits, specifically those involved in direct contact with tubulin and actin during their folding (21, 33), and in ATP consumption (22, 34, 35). The silenced T cells (siCCT-treated cells) did not correctly polymerize MTs from the centrosome, as simulated upon treatment with CHX, an inhibitor of protein synthesis.
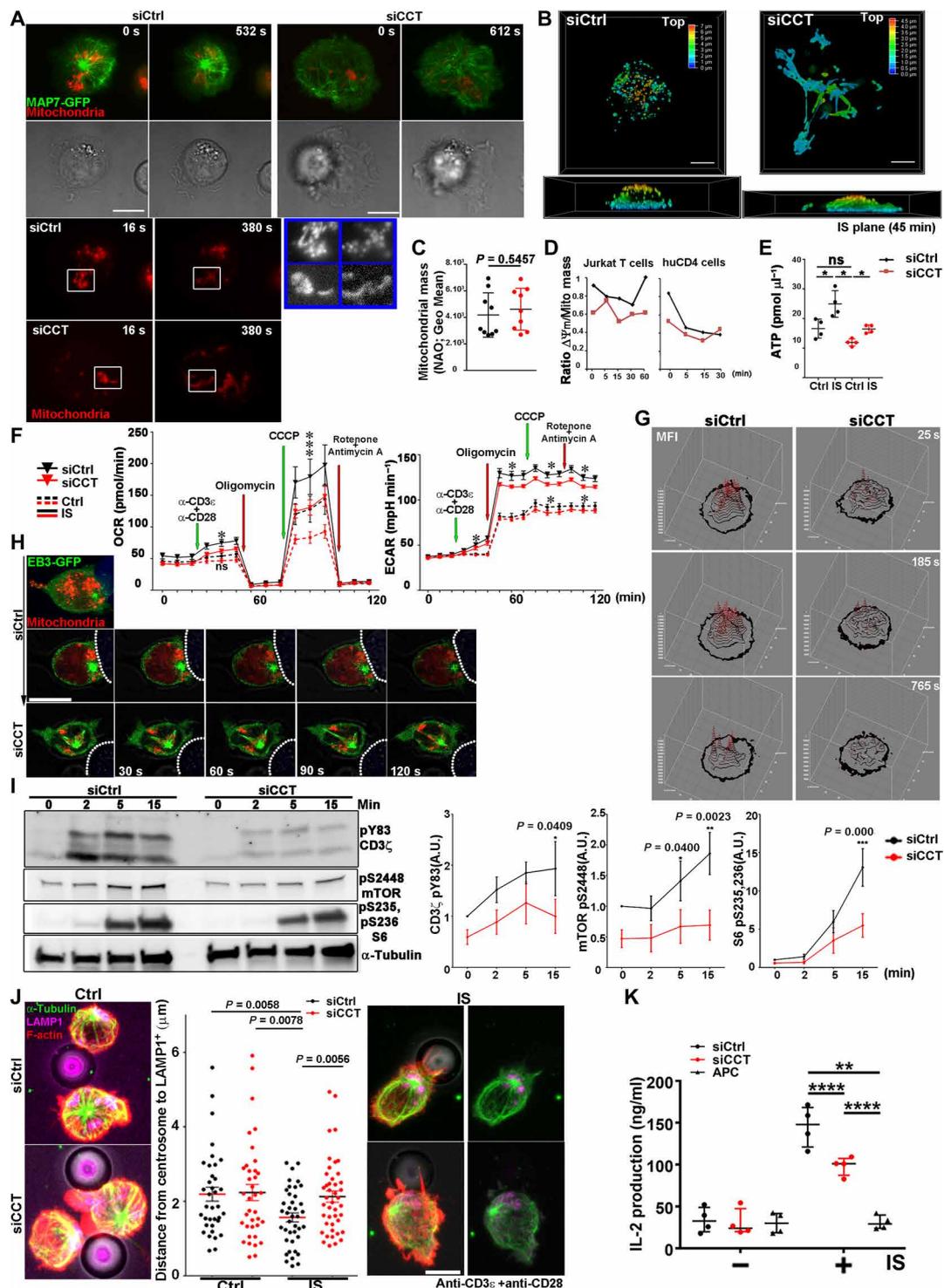
Fig. 6. CCT regulation of tubulin dynamics controls mitochondrial and metabolic tuning during IS formation. (**A**) Mitochondrial dynamics at the IS. Fluorescence (TIRFm) and bright-field (BF) images. Blue boxes, magnification of the insets (scale bars, 5 μm; $n = 4$). (**B**) STED 3D reconstruction of siCtrl and siCCT cells forming IS (45 min). Scale, distance to IS. Scale bar, 5 μm; $n = 3$. (**C**) Mitochondrial mass ($n = 8$). (**D**) Normalized ratio of mitochondrial membrane potential (ΔΨ) to total mitochondrial mass during IS. (**E**) ATP production during IS ($n = 4$; Mann-Whitney). (**F**) Mitochondrial respiration during IS ($n = 4$). (**G**) Mean fluorescence intensity (MFI) from IS-forming cells by TIRFm (Mitotracker Orange; frame lapse, 5 s; $n = 3$). (**H**) Mitochondrial localization at the IS (dotted lines, SEE-pulsed APCs). Scale bar, 10 μm. (**I**) mTORC1 signaling in human CD4 T cells. Graphs, normalized fold-induction ratios. Means ± SEM; one-way ANOVA ($n = 4$). (**J**) LAMP1⁺ vesicles in siCtrl and siCCT human CD4 T cells. Fluorescence maximal projection and BF merged image showing control or stimulating beads. Scale bar, 5 μm. Graph, LAMP1⁺ distance to the centrosome [$n = 36$ (siCtrl-Ctrl), 37 (siCCT-Ctrl), 40 (siCtrl-IS), and 43 (siCCT-IS); three donors; mean ± SD]; one-way ANOVA. (**K**) IL-2 production from siCtrl and siCCT cells ($n = 4$; one-way ANOVA; **$P < 0.01$; ****$P < 0.0001$).

The role of the centrosome in mitosis and the establishment of polarity during development is well known (*36*), and its components have been analyzed by different means including biochemical isolation and Western blot, immunofluorescence, and proteomics (*16*, *36*, *37*). In T cells, centrosome polarization and its tubulin-nucleating activity constitute important processes that lend support to specific T cell activation (*2*, *20*), thus allowing progression of adaptive immune responses. Because of the relevance of this process, we analyzed the structural organization of the IS in control and CCT KD human primary CD4 T cells from peripheral blood using a noninvasive approach. Whole cells were vitrified and subjected to cryo-SXT to generate a 3D view without any fixative, stain, or mechanical slicing, at a higher resolution than any optical microscopy (*38*). Our results allowed us to parameterize the localization and arrangement of the centrosome and centrioles at a nanometric resolution. siCCT-treated cells did not organize the area surrounding the centrosome (what we have termed AIC) and the IS, although they formed an actin lamella at the area of adhesion and polarized the centrosome.

cryo-SXT, STED, and TIRFm data showed that, although cell adhesion was conserved and cortical actin remained arranged in the characteristic lamella organized around the APC, tubulin polymerization from the centrosome was clearly disrupted after CCT KD. αβ-Tubulin polymerization increased in activated T cells, so the observed rise in the proportion of soluble heterodimers would be expected to sustain increased MT growth upon TCR activation. Nevertheless, the observed accumulation of heterodimers in CCT KD cells does not correspond with this notion. Differences in the PTM of these heterodimers upon T cell activation, altered in siCCT-treated cells, are probably the basis of the defect in tubulin polymerization. The detected lack of detyrosinated (Δ1) and Δ2 PTMs in the soluble heterodimers from siCCT cells supports that these PTMs control tubulin polymerization. Tyrosinated α-tubulin is the nonprocessed protein, which allows rapid MT depolymerization after its incorporation (*25*). This is prevented by detyrosination of α-tubulin by a carboxypeptidase (*39*), resulting Δ1-α-tubulin (glutamylated-α-tubulin), which is observed upon T cell activation [here and (*40*)]. It seems that detyrosination occurs in the polymerized MTs, allowing low rates of depolymerization. The conversion of α-tubulin into Δ2-α-tubulin has been linked to the degradation of the protein due to the nonreversible nature of this PTM; Δ2-α-tubulin accumulates in long-lived, very stable MTs but cannot be tyrosinated by the tubulin-tyrosine ligase as Δ1-α-tubulin is (*41*). The incorporation may have been short-lasting due to active MT depolymerization when CCT is not available to actively fold newly synthesized tubulin, since CCT activity is needed for tubulin folding after synthesis of the protein (*26*). Consistent with this, we reproduced a similar accumulation by inhibition of polysome-dependent ribosomal synthesis of tubulin by CHX treatment at short times (*42*), which also prevented MT growth. Conversely, we also observed that BTZ treatment induced the decrease in soluble heterodimers, accompanied by increased tubulin polymerization at the IS. The chronic inhibition of the proteasome through BTZ induces MT polymerization in other systems (*43*). Therefore, CCT accumulated in the AIC to assist in MT polymerization during the induced tubulin synthesis after TCR activation and its function seems to be coordinated with the proteasome, which is also accumulated at the AIC. The subcellular localization of CCT may represent a mechanism to control its folding activity through the availability of client proteins and co-chaperones. It is conceivable that heterodimers bearing specific PTMs such as acetylation or pE do not incorporate correctly into MTs. The increase in pE tubulins and acetylated (AcK40) α-tubulin reflects the altered MT dynamics in CCT KD cells. These are markers of MT stability (*24*), which were higher during resting state in CCT-deficient cells, the opposite of what was observed in control cells. Furthermore, T cell activation did not increase these PTMs in CCT KD cells, an observation supported by the altered binding of MAP7 to the MT network at the IS. The MT network in CCT KD T cells was "frozen" upon activation, which probably affected their ability to correctly mature their centrosomes. All this is in agreement with the altered response of the centrioles in activated siCCT-treated cells, with differential intracentrosomal disposition, with no changes in their relative angle. The centrosome localization relative to the IS plane was altered in stimulated cells by the deficiency in CCT activity, which may have prevented proper MT organization at the IS, as observed in live-cell TIRFm experiments. In control cells, the centrosome and associated GA and secretory apparatus were in close apposition to the APC.

The localization and arrangement of the centrosome is proposed to be an important factor for asymmetric division in T cells upon cognate TCR-mediated stimulation, necessary for the differentiation of naïve T cells into effector and memory T cells (*44*). However, when CCT subunits were silenced, the centrosome mislocalized and did not properly move toward the IS. This was associated with defects in the dynamics of tubulin polymerization and MT growth and in the efficient transit between the centrosomal area and the IS, which impaired the movement of CD3ζ-bearing signaling nanovesicles. Hence, the role of CCT in IS formation is related to the cytoskeleton network organization. The PCM-localized endosomes were, conceivably, the specific accumulation place of proteasome subunits, chaperones, and Rabs (Ras-associated binding proteins) for organelles with a relevant role in T cell activation and recycling of cell components. Observation of regulatory proteins of intracellular traffic in the centrosome-enriched fractions points to this location as an important hub for triage between folding and degradation at the IS. The influence of inhibitors of protein synthesis and degradation (proteasome) in tubulin dynamics supports the coordination between cell reorganization, transport, synthesis, and degradation upon TCR activation at the AIC. The dynamics of the centrosome at the IS were clearly altered when CCT activity was silenced, and the subsequent localization and movement of CD3ζ-bearing vesicles at the IS were also abolished. These events prevented the correct clustering of TCR/CD3 complex at the plasma membrane, with less protein observed. Moreover, the polarization of LAMP1⁺ vesicles was also impaired. Vesicle trafficking is dependent on MT-based intracellular transport (*20*), and defects prevent full T cell activation, as observed in CCT KD cells.

Our data show that CCT is needed for normal shape, size, and localization of mitochondria at the IS. In CCT KD cells, mitochondria were defective in their capacity to depolarize their membrane by dropping membrane potential, which is essential for correct T cell response and metabolic status. This was further corroborated by our observations that siCCT cells show a reduced OCR (an indicator of oxidative phosphorylation), a reduced ECAR (an indicator of glycolysis), and reduced ATP production upon T cell activation. Therefore, to sustain their metabolic status during activation, T cells require CCT. The calcium-dependent pathways seem to be affected by this delocalization, as observed by the decreased activation of NFATc2, corresponding to their described role in sustaining calcium flow at the IS (*11*). The mTOR complex, which is involved in mitochondrial

activation, lysosome function, and ribosomal synthesis (*45*), remained poorly active upon TCR stimulation in CCT KD cells, preventing phosphorylation and activation of the S6 ribosomal component, indicating a defective ribosomal activation. Therefore, there is a lack of protein synthesis in these cells upon activation, which is supported by the effect of inhibition through CHX, mimicking the CCT effect. Since this chaperone is in charge of folding mLST8 and Raptor, two members of the mTOR complex (*28*), a coordinated action of CCT during TCR activation would be required during IS formation to allow protein synthesis induction and folding of de novo proteins. Hence, CCT activity determines the polarization capacity of T cells during IS formation and is required to organize and allow correct function of the organelles for proper T cell activation.

In summary, we report herein, using different structural and biochemical techniques, changes in the 3D ultrastructure of the centrosome and the protein composition during IS formation in human primary CD4 T cells. We found that the metabolic status of activated T cells is dependent on this chaperone, which assists in protein synthesis and folding induced by TCR activation, directly intervening in the ability of tubulin to be incorporated and retained into MTs. These changes control and determine the organization and functionality of organelles such as mitochondria and are dependent on the chaperone CCT, which is enriched in activated centrosomes. We propose that this mechanism is relevant for biological processes undergoing cell polarity events such as embryonic development.

MATERIALS AND METHODS
Experimental design
Sample size
For experimentation performed in this work, we initially used an already known sample size that was previously used in other works for similar techniques, although performed with samples from different organisms or cells. The experiments with human primary cells were performed with the number of different donors needed to have enough biological material to perform the required techniques (biochemical extraction of samples, proteomic studies, cryo-soft x-ray microscopy, and flow cytometry). The experimental results obtained allowed the investigators to determine that the sample size was correct. Data exclusions. In general, there has not been data exclusion during the analysis of data. For proteomic and microscopic analysis, specific information is provided along individual sections here in Methods. Replication. The main conclusions and data obtained in this work have been replicated in different laboratories and investigators participating in this study; the results have been corroborated with cell lines and primary cultures. Randomization. Samples were homogeneously divided into the experimental groups in a random form for the different experiments performed (different kind of cells, primary or cell lines, were always isolated and cultured in parallel, treated similarly, and used in comparable experimental conditions). Blinding. Cells and samples were always treated and analyzed similarly, independently of their origin or category. Blinding of samples was not routinely performed but was randomly executed during different repetitions of experimentation (microscopy and proteomics), since investigators performing the different steps of experiments, such as biochemical extractions, Western blotting, microscopic analysis, or proteomic studies did not inform each other about the numbering/categories of samples until the end of the experimental repetition.

Antibodies and reagents
The source of commercial antibodies was as follows: anti-human CD3ε clone HIT3a monoclonal antibody (mAb) (BioLegend); T538 Protein kinase C (PKC-θ), Y783 PLCγ1, PLCγ1, pS2448 mTOR, mTOR, pS235-S236 S6, S6 ribosomal subunit, pS468 NFκB, pS402Y404 Erk1/2, Erk 1/2 rabbit antibodies (Cell Signaling Technology); Protein kinase C (PKC), myosin light chain (MLC), purified mouse anti-human CD28, and anti-p150 Glued mAbs (BD Biosciences); β-actin AC-15 clone, anti-γ-tubulin GTU88 clone, anti–α-tubulin DM1A clone, anti–α-tubulin–fluorescein isothiocyanate (FITC) DM1A clone, and anti-K40Acetyl–α-tubulin 12B4 clone mAbs (Sigma-Aldrich); rabbit anti-LAT and rabbit anti-Tom20 antibodies (Santa Cruz Biotechnology); anti-phosphoY132 LAT, rat anti-CCT1, rabbit anti-CCT4, rabbit anti-CCT5, rabbit anti-giantin, and chicken anti-GFP antibodies (Abcam); golgin-97 mAb (Life Technologies) and goat anti-mouse H&L chain–specific immunoglobulin G and mouse anti-CCT2 antibodies (Merck Millipore); anti-human CD28-PE, anti-LAMP1–Alexa Fluor 647, anti-human CD4 V450, anti-human CD8 V500, anti-human CD3-Allophycoerythrine, anti-human CD45RA, anti-human HLA DR-Peridinin Chlorophyll Protein, anti-human CD11a-Biotin, anti-human CD11a-allophycocyanin, anti-human CD69-allophycocyanin, and anti-human CD3ε-PE (BD Biosciences); anti-human CD3 FITC and isotype control–FITC (Immunostep); anti-pS19 MLC (Rockland Antibodies). Alexa Fluor 647 and Alexa Fluor 568 conjugated phalloidin, MitoTracker Orange and CMAC probes, Alexa Fluor 488 conjugated anti-chicken, highly cross–adsorbed Alexa Fluor 647 and Alexa Fluor 568 conjugated anti-rabbit, and Alexa Fluor 488 conjugated anti-mouse antibodies were from Molecular Probes, Invitrogen, and Thermo Fisher Scientific. The rabbit anti-CD3ζ 448 antibody was a gift from B. Alarcón [Centro de Biología Molecular "Severo Ochoa" (CBMSO), Madrid, Spain]. The rabbit anti-NFATc2 antibody was a gift from J. M. Redondo [Centro Nacional de Investigaciones Cardiovasculares (CNIC), Madrid, Spain]. Mouse monoclonal antibody clone T3b anti-human CD3ε was produced at the Immunology Department (Hospital Princesa, Madrid). Rabbit antibodies for tubulin PTMs pE-tubulin, Δ1- and Δ2-α-tubulin, and mouse anti–α-tubulin 12G10 clone and β-tubulin E7 clone were generated by I. Vernos. Anti-TBC polyclonal antibodies were generated by J. C. Zabala.

Cell lines
The Raji lymphoblastoid B and Jurkat E1-6 cell lines were grown in RPMI 1640 medium (Gibco) supplemented with 5% fetal bovine serum (FBS). The following reagents were obtained through the National Institutes of Health (NIH) AIDS Reagent Program, Division of AIDS, National Institute of Allergy and Infectious Diseases, NIH: Raji from L. Wu and V. N. KewalRaman and Jurkat from A. Weiss. Medium for CH7C17 Jurkat T cells stably expressing TCRvβ3 specific for a peptide from influenza hemagglutinin (HA) was supplemented with hygromycin (400 μg/ml) and puromycin (4 μg/ml) (Invivogen). Geneticin-418 (0.4 mg/ml; Invivogen) was added for culturing CH7C17 T cells stably transfected with MAP7-GFP, EB3-GFP, and EB3-RFP constructs [EB3 constructs were from A. Akhmanova (Utrecht University, Netherlands)]. Both Raji and Jurkat cells come from NIH AIDS Reagent Program and show XY genotype.

Primary human lymphocytes
For isolation of CD4 T cells or T lymphoblast cultures, human peripheral blood mononuclear cells (PBMCs) were isolated from buffy coats from healthy donors [provided by "Centro de Transfusiones

de la Comunidad de Madrid" under an agreement with the Hospital Princesa (Madrid) and approved by the CEIm of Hospital Princesa, according to government ethical consent] through separation on a Biocoll gradient (Biochrom). Nonadherent cells were collected after plating PBMCs at 37°C. CD4 T cells for synchrotron experiments were isolated with a Miltenyi Biotec negative isolation kit or with a STEMCELL negative isolation kit and used for subsequent procedures. Peripheral blood lymphocytes obtained after adhesion steps were cultured for 48 hours in the presence of SEE (0.01 μg/ml; Toxin Technology) to induce lymphocyte proliferation, and IL-2 (50 U/ml) was added to the culture medium every 2 days until use. Further information and requests for resources and reagents should be directed to and will be fulfilled by corresponding authors.

Cell transfection

CH7C17 or E1-6 Jurkat T cells (1.5×10^7) were transfected with 1.2 μM of each siRNA to a total 5 μM and 3.5 μg of plasmid using the Gene Pulser II (Bio-Rad) at 240 V and 975 μF, and cells were analyzed 48 hours after transfection. Primary CD4 T cells were nucleofected with Amaxa I in Opti-MEM I (Gibco, Invitrogen) using U-04 program after a heat-shock step with HBSS (Hank's buffered salt solution). Cells were cultured for 48 hours in RPMI 1640 supplemented with 10% FBS and IL-7 (10 ng/ml).

T cell activation, cell lysis, SDS- and native-PAGE, and immunoblotting

For human TCR stimulation, T cells were incubated for the indicated times with latex microbeads (6.4 μm in diameter) conjugated to anti-CD3ε mAb (5 μg/ml) and anti-CD28 mAb (1.66 μg/ml). Cells were activated with anti-CD3ε + anti-CD28–coated beads to avoid the presence of tubulin from APCs in the cell lysates. T cells were incubated for the indicated times allowing them to spread over surfaces coated with anti-CD3ε mAb (5 μg/ml) and anti-CD28 mAb (1.66 μg/ml). For antigen stimulation, Raji cells were pulsed with SEE (0.3 μg/ml, 30 min) and mixed with Jurkat cells (1:10); alternatively, Hom2 cells pulsed with HA peptide (200 μg/ml, 2 hours) or with SEB (5 μg/ml, 30 min) were mixed with CH7C17 cells (1:10) in HBSS. Where indicated, cells were pretreated with BTZ (520 nM, 2 hours; Calbiochem), CHX (20 μg/ml, 40 min; Sigma-Aldrich), or vehicle at 37°C in HBSS before stimulation. For SDS–polyacrylamide gel electrophoresis (PAGE), cells were lysed in 20 mM tris-HCl (pH 7.5) containing 1% NP-40, 0.2% Triton X-100, 150 mM NaCl, 2 mM EDTA, 1.5 mM MgCl$_2$, and phosphatase and protease inhibitors. Lysates were spun at 1000g (4°C, 10 min) to remove debris and nuclei. Proteins were resolved by SDS-PAGE and transferred to nitrocellulose membranes. For NFAT analysis, 6% polyacrylamide gels containing 1 mM EGTA were used. After blocking with tris-buffered saline (TBS) containing 0.2% Tween and 5% bovine serum albumin (BSA), membranes were blotted with primary antibodies (overnight at 4°C) and peroxidase-labeled secondary antibodies (30 min) and detected with the ImageQuant LAS-4000 chemiluminescence and fluorescence imaging system (Fujifilm). For native-PAGE assays of protein complexes, cells were resuspended in 0.1 MES (pH 6.7) containing 1 mM EGTA, 1 mM MgCl$_2$, 10 mM guanosine 5′-triphosphate (GTP), inhibitors of proteases and phosphatases, lysed through a 2-ml dounce homogenizer (20 strokes; tight pestle) at room temperature and centrifuged at 14,000g at 25°C for 30 min. Protein content in supernatants was determined by Bradford assay, and native electrophoresis was performed for 2 hours at 80 V in MES buffer containing 1 mM MgCl$_2$, 1 mM EGTA, and 1 mM GTP. Samples were run in triplicate with

20 μg loaded per sample and transferred to nitrocellulose membranes for 2 hours at 400 mA in tris-Gly solution. Blots were probed against the indicated antibodies; anti-TBCs were used at 1:1500, anti-tubulins at 1:10,000, and anti-PTMs at 1:2000 (46).

Centrosome-enriched subcellular fraction isolation

Primary human T lymphoblasts were stimulated with anti-CD3ε + anti-CD28–coated beads for 20 min, ice-cooled, and centrifuged at 2,000g at 25°C for 30 min. Cells were washed in TBS and resuspended in lysis buffer (2×10^6 cells/ml) 1 mM tris-HCl (pH 7.4) containing 0.5% NP-40, 0.5 μM MgCl$_2$, 0.1% β-mercaptoethanol, and inhibitors of proteases and phosphatases for 10 min with gentle shaking. Lysates were filtered through a nylon mesh and centrifuged at 24,000g with inhibitors for 10 min at 4°C. The supernatant was filtered again to re-equilibrate it into a final 10 mM piperazine-N,N'-bis(2-ethanesulfonic acid) (PIPES) (pH 7.2) and then centrifuged to pellet the centrosomes (24,000g at 4°C for 60 min). The pellet was resuspended in 10 ml of gradient buffer [10 mM PIPES (pH 7.2), 5% sucrose, 0.1% β-mercaptoethanol, and 0.1% Triton X-100] and homogenized through 21-gauge (two times) and 25-gauge (three times) needles before loading onto the first sucrose gradient [1 ml 70%, 2 ml 50%, 2 ml 40%, 2 ml 30%, and 2 ml 20% (w/w)]. The gradient was subjected to a 32,500g centrifugation for 1 hour at 4°C in an SW28 rotor. Fractions from 50 to 70% were collected, mixed, diluted with gradient buffer to a final concentration of about 20 to 30% of sucrose and loaded onto a second sucrose gradient [0.5 ml 70%, 0.5 ml 50%, and 1 ml 40% (w/w)]. The gradient was centrifuged at 130,000g for 1 hour at 4°C in an SW40 Ti rotor, and fractions were then recovered and analyzed for γ-tubulin content by Western blot and immunofluorescence and for in vitro tubulin polymerization ability. Centrosome-enriched fractions from Jurkat T cells were isolated as described (16) in similar resting and activation conditions to the primary T lymphoblasts and analyzed as above to determine γ-tubulin–enriched fractions. Proteomic analysis was performed from equivalent enriched fractions.

In vitro polymerization of tubulin

Rhodamine-conjugated αβ-tubulin and nonlabeled αβ-tubulin were resuspended in 80 mM PIPES buffer (pH 6.9) containing 1 mM MgCl$_2$, 1 mM EGTA, 5% glycerol, and 1 mM GTP. Dissolved tubulins were stored at 5 mg/ml and mixed 1:5 for polymerization (2.86 mg/ml, 10 μl) with centrosome fractions (2.5 μl) and 5 μl of buffer. Tubes were heated at 37°C for 20 min, and reactions were stopped by glutaraldehyde fixation (1%) for 5 min at 37°C. Samples were then diluted in 80 mM PIPES buffer (pH 6.9) containing 10 μM taxol, 1 mM MgCl$_2$, and 1 mM EGTA for additional 5 min before spinning them onto acid-washed coverslips (thickness of 1.5 H) on a glycerol cushion for 30 min at 30°C. Coverslips were fixed in methanol for 5 min at −20°C and stained for γ-tubulin (1:200; 1.5 hours, 37°C; GTU88) and analyzed with a SP5 Leica confocal microscope.

Mitochondrial depolarization assay

T cells nucleofected with siCtrl or siCCT were sorted and stained with MitoTracker Orange (1 μM; Molecular Probes/Invitrogen/Thermo-Fisher Scientific) for 1 hour at 37°C and stimulated with anti-CD3ε + anti-CD28–coated beads for the times indicated, cooled on ice, fixed, stained for Tom20 (total mitochondrial mass), and analyzed by flow cytometry. Ratio of MitoTracker: Mitochondrial mass was calculated for each time point. Mean fluorescence intensity and Geo Mean of staining were analyzed with a LSRFortessa flow cytometer (BD Biosciences) and FlowJo v10.1 software (TreeStar).

Mitochondrial stress test

To measure the bioenergetics of the cells, siCtrl or siCCT human primary CD4 cells were cultured on Dulbecco's modified Eagle's medium (four donors, five replicates) on XFe96 FluxPak (Agilent Technologies) following the manufacturer's instructions. Respiration was measured with an XFe96 extracellular flux analyzer (Seahorse Bioscience). Cells were seeded at 0.8×10^6 per well and activated with anti-CD3ε + anti-CD28 tetramers (25 μl/10^6 cells; Stem Cell). Drugs were injected as follows: oligomycin (1 μM), Carbonyl Cyanide m-chlorophenylhydrazine (CCCP) (1.5μM), rotenone (1 μM), and antimycin A (1 μM). Results were analyzed with Seahorse Wave software and subjected to a linear mixed model statistical analysis (R 3.6.3 version; https://stats.idre.ucla.edu/other/mult-pkg/introduction-to-linear-mixed-models/).

ATP fluorometric assay

To measure ATP content, 3.10^6 siCtrl or siCCT human primary CD4 cells were activated with anti-CD3ε + anti-CD28 tetramers (15 μl/10^6 cells; Stem Cell) and lysed in ATP assay buffer from an ATP assay kit (Abcam ab83355), deproteinized with 4 M perchloric acid, and neutralized with 2 M KOH. Samples were cold-iced throughout the process. Enzymatic reactions were performed following the manufacturer's instructions, and fluorometric assays were read with a Fluoroskan Ascent (ThermoLabsystem).

Flow cytometry, sorting, and ELISA

Cell conjugates were allowed to form for 18 hours, and supernatants and cells were collected for enzyme-linked immunosorbent assay (ELISA) and flow cytometry, respectively. A specific ELISA detection kit (DiaClone) was used to quantify the levels of IL-2 secreted, and colorimetric intensity levels were detected on a Bio-Rad plate reader with a 450-nm filter. For flow cytometry analysis, staining was performed with anti-human CD69-allophycocyanin (BD Biosciences) and anti-human CD3ε-phycoerythrin (PE) in fluorescence-activated cell sorting (FACS) blocking solution [1% BSA, 1% FBS, human γ-globulin (100 μg/ml), and 0.01% sodium azide in PBS] for 30 min at 4°C. Other stainings were as follows: CD4 purification control: anti-human CD19-PE, CD8-V500, CD4-V450, DR-perCP, CD3-APC, CD45Ro-Cy7, and CD45RA-FITC; CD3 surface expression: anti-human CD3ε-FITC or isotype control-FITC, CD28-PE, and CD11a allophycocyanin; anti-human CD3ε (T3b) or control X63 clone, anti-mouse-allophycocyanin; and anti-CD28-PE. Mitochondrial mass was assessed in cells labeled with nonyl-acridine orange (25 nM) for 15 min at room temperature and stained for CD3-allophycocyanin (4°C). Cell viability assays were performed with the Annexin V–CF Blue/7-aminoactinomycin D (7-AAD) Apoptosis Detection kit (Abcam ab214663), following the manufacturer's instructions. Mean fluorescence intensity and Geo Mean of staining were analyzed with a FACS-Canto II 3L, a FCAS-Canto II HTS or a LSR Fortessa flow cytometer with FACSDiva software (BD Biosciences), and FlowJo v10.1 software (TreeStar). Sorting was performed by separating GFP⁺ cells in a digital flow sorter FACSAria Cytometer with FACSDiva software (BD Biosciences) 48 hours after transfection.

STED, time-lapse confocal and TIRFm videos

STED images were acquired using a Leica SP8 gSTED 3D system equipped with a pulsed white light laser (WLL; range, 470 to 670 nm) as an excitation source and 660 or 592 nm as the STED depletion sources. All images were acquired using a HC PL Apo CS2 100×/1.4 oil objective and accompanying Application Suite X software (LAS X, 3.5.2. 18963; Leica Microsystems GmbH). Line scan speed of 1000 Hz

was used, combined with bidirectional scanning. Alexa 488 [chicken anti-GFP (Abcam) plus Alexa 48–conjugated anti-chicken (Invitrogen) antibodies] and MitoTracker Orange or Alexa 568 [anti-Giantin (Abcam) plus Alexa 568–conjugated anti-rabbit antibodies] were imaged with 488- and 568-nm excitation and 592- and 660-nm depletion wavelengths, respectively. The depletion laser power was 111 mW. Alexa 647–conjugated phalloidin fluorescence was acquired in confocal mode. Fluorescence-emitted light was collected with HyD hybrid detectors for all fluorochromes. Image processing was performed with Fiji software (ImageJ) for fluorescence images and 3D reconstruction and with Imaris software for detection of volumes and 3D reconstruction in the case of Jurkat T cell line and SEE-pulsed Raji (APCs) conjugates. The 3D rendering mode from LAS X software 4.0.0.11706 (Leica Microsystems GmbH) was used for volume reconstructions of mitochondria in Jurkat T cells forming IS on stimulating surfaces. For cell conjugates, 4D imaging was performed using 5×10^5 CMAC (7-amino-4-chloromethylcoumarin)–loaded Raji APCs [SEE-pulsed (E1-6 Jurkat cells), SEB-pulsed (CH7C17 Jurkat cells), or unpulsed] allowed to adhere to fibronectin-coated glass-bottom 35-mm dishes (no. 1.5; MatTek Corporation, Ashland, MA, USA). Cells were maintained in 2 ml of HBSS containing 1% FBS and 25 mM Hepes. T cells were added (1:1 ratio), and a series of fluorescence and bright-field frames were captured using a TCS SP5 confocal laser scanning unit (Leica Microsystems) attached to an inverted epifluorescence microscope (DMI6000) fitted with an HCX PL Apo 63×/1.40 to 0.6 oil objective. Images were acquired and processed with the accompanying Leica confocal software (LCS; Leica microsystems, GmbH) and ImageJ software (http://rsbweb.nih.gov/ij/). A Leica SP8 Navigator confocal microscope equipped with a pulsed WLL (range, 470 to 670 nm) and an HC PL Apo CS2 100×/1.4 oil objective and accompanying Application Suite X software (LAS X, 3.5.2. 18963; Leica Microsystems GmbH) was used to acquire the confocal images for fixed cell conjugates of Jurkat T cells and Raji cells (CMAC-labeled and pulsed or not with SEE and stained for CD3ε). For 4D resonant scanning rapid acquisition of EB3-GFP–transfected cells, the TCS SP5 confocal laser scanning unit (Leica Microsystems) was used in resonant scanner mode, with 1 to 2 s for each Z-scan, allowing whole-cell recording. Bright-field images and fluorescence images were acquired. For TIRFm, T cells transfected with corresponding siRNAs, EB3-GFP, EB3-RFP, CD3ζ-mCherry, or MAP7-GFP were allowed to settle onto glass-bottom dishes coated with anti-CD3ε (10 μg/ml) and anti-CD28 (3 μg/ml). For cells pretreated with CHX (20 μg/ml for 40 min) or BTZ (520 nM for 2 hours), the drug was maintained in the imaging medium during acquisition. Recording was initiated 3 min after cells were plated, and cells were visualized with a Leica AM TIRF MC M system mounted on a Leica DMI6000B microscope coupled to an Andor-DU8285_VP-4094 camera fitted with a HCX PL Apo 100.0×/1.46 oil objective. Images were processed with the accompanying confocal software (LCS; Leica). Time-lapse settings were optimized for each type of experiment and are specified throughout the text. The laser penetrance used was 150 nm for both laser channels (488 and 561 nm). Synchronization was performed with the accompanying Leica software, and images were processed with Leica software and ImageJ software (http://rsbweb.nih.gov/ij/).

cryo-SXT data acquisition and image processing

Isolated peripheral blood CD4 cells from healthy donors or Jurkat T cells were cotransfected with EB3-GFP and the corresponding siRNAs (siCtrl or siCCT) and treated with IL-7 for survival for 48 hours.

GFP+ cells were sorted and subsequently incubated for 20 min with MitoTracker Red to label mitochondria (facilitating correlative microscopy and fast cryo-epifluorescent analysis of the grid quality). After that, 10^4 cells were deposited on specific stimulating-layer grids to form an IS. The stimulating surface used was similar to the one used for TIRFm (20). Holey carbon–coated (R 2/2; Quantifoil) Au-electron microscopy (EM) finder grids were incubated for 8 hours at 4°C with activated α-CD3ε (20 μg/ml) and α-CD28 (3 μg/ml) antibodies to generate a stimulating carbon surface. For control grids without stimuli, carbon surface was incubated with poly-L-lysine. Cells were incubated for 20 min at 37°C over the corresponding type of grid surface and fixed by plunge-freezing in an EM CPC vitrification unit (Leica Microsystems). Grids were maintained in liquid nitrogen during the whole process. Vitrified grids were first analyzed at liquid nitrogen temperature with the cryo-correlative cooling stage (Linkam Scientific Instruments). The cryo-stage was then inserted into an AxioScope A1 (Carl Zeiss) epifluorescence microscope with an N-Achroplan 10×/0.25 Ph1 objective and imaged with a charge-coupled device (CCD) AxioCam ICm1 (Carl Zeiss).

Samples were previsualized with a visible light microscope on-line within the x-ray microscope to correlate cell position with epifluorescence and cryo-epifluorescence images. At the Mistral beamline (ALBA Synchrotron), zero degree soft x-ray projection mosaics were acquired to evaluate sample conditions (vitrification and thickness). Tilt series were acquired at 520-eV photon energy from −65° to 65° at 1° intervals, using a 25-nm zone plate. To avoid depth of focus artifacts, the x-ray tomography enhanced defocus (XTEND) scheme (38) was used to acquire tilt series. Exposure time depended on sample thickness and ranged in our work from 1 to 4 s. The final image pixel size was 10 nm. We used a beam time of 5 days corresponding to 15 shifts at the Mistral microscope placed in the ALBA Synchrotron. We acquired 48 XTEND1 datasets per cell (one dataset is equal to three inclined series). The 48 datasets from single cells corresponded to 16 siCtrl resting cells, 9 siCtrl cells forming IS, 13 siCCT resting cells, and 10 siCCT cells forming IS. To monitor experimental resolution of the tomograms, we used Nyquist criteria associated with the line spread function.

Protein digestion, peptide labeling, and fractionation for proteomics

For label-free experiments, centrosomal-enriched fractions from resting or activated Jurkat T cells were isolated as described in (16), and two biological replicates were analyzed for protein content. Centrosomal-enriched fractions from resting or activated T lymphoblasts from healthy donors were processed as described and subjected to iTRAQ. For isobaric labeling, three different experiments, each comprising two biological replicates for each condition, were analyzed in three independent iTRAQ 4-plex experiments. Proteins for label-free or iTRAQ analysis were digested using the in-gel digestion protocol as previously described (47), with some modifications. Briefly, supernatants were run by conventional SDS-PAGE until the front entered the resolving gel. The protein band containing the whole proteome was visualized by colloidal Coomassie staining, destained with water, and bands were excised and cut into cubes. Samples were subjected to reduction with 10 mM dithiothreitol and alkylation in 50 mM iodoacetamide and digested overnight at 37°C with modified trypsin (60 ng/ml; Promega, Madison, WI, USA) at a 12:1 protein:trypsin (w/w) ratio in 50 mM ammonium bicarbonate (pH 8.8) containing 10% acetonitrile. The resulting tryptic peptides were extracted by incubation in 12 mM ammonium bicarbonate (pH 8.8) and, later,

0.5% TFA (trifluoroacetic acid), which was added at a final concentration of 1%, and the peptides were lastly desalted in C18 Oasis-hydrophilic-lipophilic-balanced (HLB) cartridges and dried-down for further analysis.

For stable isobaric labeling, the resulting tryptic peptides were dissolved in 500 mM triethylammonium bicarbonate buffer, and the concentration of peptides was determined by measuring amide bonds with the Direct Detect system (Millipore). Equal amounts of each peptide sample were labeled using the 4-plex iTRAQ Reagents Multiplex Kit (Applied Biosystems, Foster City, CA, USA) according to the manufacturer's protocol. Each peptide solution was independently labeled with one iTRAQ reagent vial previously reconstituted in isopropanol. After incubation at room temperature for 1 hour, the reaction was stopped with 0.5% TFA, incubated for 15 min, and peptides were combined. Samples were concentrated in a Speed Vac, desalted in C18 Oasis-HLB cartridges, and dried-down for further analysis. For increasing proteome coverage, iTRAQ-labeled samples were separated into four fractions by mixed-cation exchange chromatography (Oasis HLB-MCX columns), which were desalted before tandem mass spectrometry (MS/MS) analysis. For label-free experiments, the resulting tryptic peptide mixtures were dissolved in 0.5% TFA for MS/MS analysis.

LC-MS analysis

Labeled peptides were loaded into the liquid chromatography–MS/MS (LC-MS/MS) system for on-line desalting in C18 cartridges and analyzed by LC-MS/MS using a C-18 reversed phase nanocolumn (75 μm internal diameter × 50 cm; 2 μm particle size; Acclaim PepMap rapid separation liquid chromatography (RSLC), 100 C18; Thermo Fisher Scientific) in a continuous acetonitrile gradient consisting of 0 to 30% B in 360 min, 50 to 90% B in 3 min (A = 0.5% formic acid; B = 90% acetonitrile and 0.5% formic acid). A flow rate of 200 ml/min was used to elute peptides from the reversed-phase (RP) nanocolumn to an emitter nanospray needle for real-time ionization and peptide fragmentation on a Q Exactive mass spectrometer (Thermo Fisher Scientific). An enhanced Fourier Transform (FT)–resolution spectrum (resolution = 70,000) followed by MS/MS spectra from the 20 most intense parent ions were analyzed along the chromatographic run. Higher-energy collisional dissociation (HCD) fragmentation was performed at 30% of normalized collision energy and 17,500 resolution; dynamic exclusion was set at 30 s.

Database search

For isobaric labeling experiments, all searches were performed with Proteome Discoverer (version 1.4, Thermo Fisher Scientific) using SEQUEST (Thermo Fisher Scientific) against a UniProt database containing all sequences from human (March 2013; 70,136 entries), supplemented with 47 sequences from the cRAP (common Repository of Adventitious Proteins) database, containing the most common laboratory protein contaminants (Global Proteome Machine). For database searching, parameters were selected as follows: trypsin digestion with two maximum missed cleavage sites, precursor mass tolerance of 2 Da, and fragment mass tolerance of 30 ppm. Methionine oxidation (+15.994915) was set as a variable modification, whereas lysine and peptide N-terminal modification (+144.102063 Da), and cysteine carbamidomethylation (+57.021464) were set as fixed modifications. The same collections of MS/MS spectra were also searched against inverted databases constructed from the same target databases. Peptide identification from MS/MS data was performed using the

probability ratio method. False discovery rate (FDR) of the peptide identifications was calculated using the refined method; 1% FDR was used as a criterion for peptide identification. Each peptide was assigned only to the best protein proposed by the Proteome Discoverer algorithm.

For label-free experiments, tandem mass spectra and charge state deconvolution were extracted by Proteome Discoverer version 1.4 using SEQUEST (Thermo Fisher Scientific) and X! Tandem [The global proteome machine (GPM), thegpm.org; version 2007.01.01.1]. SEQUEST was set up to search MSIPI_human_3.67. fasta (87040 entries) assuming trypsin. X! Tandem was set up to search a subset of the MSIPI_human_3.67 database also assuming trypsin. SEQUEST and X! Tandem were searched with a fragment ion mass tolerance of 30 ppm and a parent ion tolerance of 15 ppm. Iodoacetamide derivative of cysteine was specified in SEQUEST and X! Tandem as a fixed modification. Deamidation of asparagine and glutamine and oxidation of methionine were also specified as variable modifications. Scaffold (version Scaffold_4.6.1, Proteome Software Inc., Portland, OR) was used to validate MS/MS-based peptide and protein identifications. Peptide identifications were accepted if they could be established at greater than 95.0% probability by the Peptide Prophet algorithm. Protein identifications were accepted if they could be established at greater than 99.0% probability and contained at least one identified peptide. Protein probabilities were assigned by the Protein Prophet algorithm. Proteins that contained similar peptides and could not be differentiated on the basis of MS/MS analysis alone were grouped to satisfy the principles of parsimony.

Peptide quantification and statistical analysis

In the isobaric labeling experiments, quantitative information from MS/MS spectra was extracted from msf files using an in-house SQLite script. The quantitative information was integrated from the spectrum level to the peptide level and then to the protein level on the basis of the weighted spectrum, peptide and protein (WSSP) model (48), using the generic integration algorithm. Briefly, for each sample i, the values $x_{\text{qps}} = \log_2 A_i/C$ were calculated, where A_i is the intensity of the iTRAQ reporter corresponding to activated sample i in the MS/MS spectrum s coming from peptide p and protein q, and C is the intensity of the iTRAQ reporter from the corresponding control sample. The $\log_2$ ratio of each peptide (x_{qp}) was calculated as the weighted average of its spectra, the protein values (x_q) were the weighted average of its peptides, and the grand mean ($\bar{x}$) was calculated as the weighted average of all the protein values (48). The statistical weights of spectra, peptides, and proteins (w_{qps}, w_{qp}, and w_q, respectively), and the variances at each of the three levels (σ_S^2, σ_P^2, and σ_Q^2, respectively) were calculated as described (48). Protein quantifications were further integrated among the six comparisons, obtaining averaged values (x_q') with their corresponding weights (w_q') for every protein (48). The Systems Biology analysis was performed according to the SBT approach (19). Briefly, averaged proteins were grouped into functional categories using Ingenuity Knowledge Database (IPA), CORUM, and DAVID. For each category, the $\log_2$ ratio (x_c) was calculated as the weighted average of its proteins, and the statistical weights (w_c) of categories were calculated as previously described (19). Protein-to-category outliers were removed at 1% FDR to end up with categories containing proteins with a coordinated behavior (19). Significant abundance changes of proteins or categories in the activated samples compared to controls were detected at 1% FDR.

SXT image quantification and statistical analysis

Automatic tilt-series preprocessing was performed following the previously described procedure (38). Integrated tilt series were aligned with IMOD and reconstructed with TOMO3D software (30 iterations of the SIRT algorithm). Semiautomatic segmentation of volumes was carried out with SuRVoS, and volumes were represented with Chimera. PCM and Mitochondrial statistics are calculated from segmented data. Centriolar angles and distances were calculated from 3D centriolar coordinates. Two points, placed in upper and lower center of the cylinder, determine the length and centriolar vector, while four points, perpendicular to this vector on the centriolar wall, were used to calculate the cylinder radius. In addition, four markers pointed to carbon surface to calculate A and alpha angles and D distance. Statistical analyses were performed using in-house Python scripts (Anaconda Software Distribution; versions 2 to 2.4.0. Anaconda Inc., November 2017; https://anaconda.com).

Quantification of microtubule plus-ends (TIPs) and vesicles through TIRFm

Acquisition and quantification as well as statistical analysis was performed as described in (49) for MT growth and vesicle traffic at the IS.

Densitometry analysis and quantification of Western blot

Bands from Western blots were analyzed with accompanying software Image Gauge (Fujifilm Inc). Background was subtracted, and arbitrary unit per pixel was normalized to control samples, not stimulated. Values were analyzed with GraphPad for significance.

General statistical analysis

Statistical significance of difference in values was calculated by parametric or nonparametric test, either analysis of variance (ANOVA), Kruskal-Wallis, Student's t test, or Mann-Whitney, where applicable, upon normal distribution analysis, or when $n < 30$. P values are denoted as follows: $*P < 0.05$, $**P < 0.01$, $***P < 0.001$, and $****P < 0.0001$. Exact P values are also indicated in the figures (Python Software and Prism, GraphPad).

SUPPLEMENTARY MATERIALS

REFERENCES AND NOTES

1. S. Petry, A. C. Groen, K. Ishihara, T. J. Mitchison, R. D. Vale, Branching microtubule nucleation in *Xenopus* egg extracts mediated by augmin and TPX2. *Cell* **152**, 768–777 (2013).
2. N. B. Martín-Cófreces, J. Robles-Valero, J. R. Cabrero, M. Mittelbrunn, M. Gordón-Alonso, C.-H. Sung, B. Alarcón, J. Vázquez, F. Sánchez-Madrid, MTOC translocation modulates IS formation and controls sustained T cell signaling. *J. Cell Biol.* **182**, 951–962 (2008).
3. A. Kupfer, G. Dennert, Reorientation of the microtubule-organizing center and the Golgi apparatus in cloned cytotoxic lymphocytes triggered by binding to lysable target cells. *J. Immunol.* **133**, 2762–2766 (1984).
4. J. C. Stinchcombe, E. Majorovits, G. Bossi, S. Fuller, G. M. Griffiths, Centrosome polarization delivers secretory granules to the immunological synapse. *Nature* **443**, 462–465 (2006).
5. M. Mittelbrunn, C. Gutiérrez-Vázquez, C. Villarroya-Beltri, S. González, F. Sánchez-Cabo, M. Á. González, A. Bernad, F. Sánchez-Madrid, Unidirectional transfer of microRNA-loaded exosomes from T cells to antigen-presenting cells. *Nat. Commun.* **2**, 282 (2011).
6. D. Sancho, M. Vicente-Manzanares, M. Mittelbrunn, M. C. Montoya, M. Gordón-Alonso, J. M. Serrador, F. Sánchez-Madrid, Regulation of microtubule-organizing center orientation and actomyosin cytoskeleton rearrangement during immune interactions. *Immunol. Rev.* **189**, 84–97 (2002).

7. M. L. Dustin, D. Depoil, New insights into the T cell synapse from single molecule techniques. *Nat. Rev. Immunol.* **11**, 672–684 (2011).

8. T. S. Gomez, D. D. Billadeau, T cell activation and the cytoskeleton: You can't have one without the other. *Adv. Immunol.* **97**, 1–64 (2008).

9. N. B. Martín-Cófreces, F. Baixauli, F. Sánchez-Madrid, Immune synapse: Conductor of orchestrated organelle movement. *Trends Cell Biol.* **24**, 61–72 (2014).

10. F. Baixauli, N. B. Martín-Cófreces, G. Morlino, Y. R. Carrasco, C. Calabia-Linares, E. Veiga, J. M. Serrador, F. Sánchez-Madrid, The mitochondrial fission factor dynamin-related protein 1 modulates T-cell receptor signalling at the immune synapse. *EMBO J.* **30**, 1238–1250 (2011).

11. A. Quintana, C. Pasche, C. Junker, D. Al-Ansary, H. Rieger, C. Kummerow, L. Nuñez, C. Villalobos, P. Meraner, U. Becherer, J. Rettig, B. A. Niemeyer, M. Hoth, Calcium microdomains at the immunological synapse: How ORAI channels, mitochondria and calcium pumps generate local calcium signals for efficient T-cell activation. *EMBO J.* **30**, 3895–3912 (2011).

12. I. G. Muñoz, H. Yébenes, M. Zhou, P. Mesa, M. Serna, A. Y. Park, E. Bragado-Nilsson, A. Beloso, G. de Cárcer, M. Malumbres, C. V. Robinson, J. M. Valpuesta, G. Montoya, Crystal structure of the open conformation of the mammalian chaperonin CCT in complex with tubulin. *Nat. Struct. Mol. Biol.* **18**, 14–19 (2011).

13. N. Kalisman, C. M. Adams, M. Levitt, Subunit order of eukaryotic TRiC/CCT chaperonin by cross-linking, mass spectrometry, and combinatorial homology modeling. *Proc. Natl. Acad. Sci. U.S.A.* **109**, 2884–2889 (2012).

14. A. Leitner, L. A. Joachimiak, A. Bracher, L. Mönkemeyer, T. Walzthoeni, B. Chen, S. Pechmann, S. Holmes, Y. Cong, B. Ma, S. Ludtke, W. Chiu, F. U. Hartl, R. Aebersold, J. Frydman, The molecular architecture of the eukaryotic chaperonin TRiC/CCT. *Structure* **20**, 814–825 (2012).

15. S. Komesli, F. Tournier, M. Paintrand, R. L. Margolis, D. Job, M. Bornens, Mass isolation of calf thymus centrosomes: Identification of a specific configuration. *J. Cell Biol.* **109**, 2869–2878 (1989).

16. M. Bornens, M. Moudjou, Studying the composition and function of centrosomes in vertebrates. *Methods Cell Biol.* **61**, 13–34 (1999).

17. L. Skjærven, J. Cuellar, A. Martinez, J. M. Valpuesta, Dynamics, flexibility, and allostery in molecular chaperonins. *FEBS Lett.* **589**, 2522–2532 (2015).

18. M. Serna, G. Carranza, J. Martín-Benito, R. Janowski, A. Canals, M. Coll, J. C. Zabala, J. M. Valpuesta, The structure of the complex between α-tubulin, TBCE and TBCB reveals a tubulin dimer dissociation mechanism. *J. Cell Sci.* **128**, 1824–1834 (2015).

19. F. García-Marqués, M. Trevisan-Herraz, S. Martínez-Martínez, E. Camafeita, I. Jorge, J. A. Lopez, N. Méndez-Barbero, S. Méndez-Ferrer, M. A. Del Pozo, B. Ibáñez, V. Andrés, F. Sánchez-Madrid, J. M. Redondo, E. Bonzon-Kulichenko, J. Vázquez, A novel systems-biology algorithm for the analysis of coordinated protein responses using quantitative proteomics. *Mol. Cell. Proteomics* **15**, 1740–1760 (2016).

20. N. B. Martín-Cófreces, F. Baixauli, M. J. López, D. Gil, A. Monjas, B. Alarcón, F. Sánchez-Madrid, End-binding protein 1 controls signal propagation from the T cell receptor. *EMBO J.* **31**, 4140–4152 (2012).

21. O. Llorca, J. Martín-Benito, M. Ritco-Vonsovici, J. Grantham, G. M. Hynes, K. R. Willison, J. L. Carrascosa, J. M. Valpuesta, Eukaryotic chaperonin CCT stabilizes actin and tubulin folding intermediates in open quasi-native conformations. *EMBO J.* **19**, 5971–5979 (2000).

22. M. Chagoyen, J. L. Carrascosa, F. Pazos, J. M. Valpuesta, Molecular determinants of the ATP hydrolysis asymmetry of the CCT chaperonin complex. *Proteins* **82**, 703–707 (2014).

23. T. Stepanova, J. Slemmer, C. C. Hoogenraad, G. Lansbergen, B. Dortland, C. I. De Zeeuw, F. Grosveld, G. van Cappellen, A. Akhmanova, N. Galjart, Visualization of microtubule growth in cultured neurons via the use of EB3-GFP (end-binding protein 3–green fluorescent protein). *J. Neurosci.* **23**, 2655–2664 (2003).

24. Y. Song, S. T. Brady, Post-translational modifications of tubulin: Pathways to functional diversity of microtubules. *Trends Cell Biol.* **25**, 125–136 (2015).

25. L. Peris, M. Wagenbach, L. Lafanechère, J. Brocard, A. T. Moore, F. Kozielski, D. Job, L. Wordeman, A. Andrieux, Motor-dependent microtubule disassembly driven by tubulin tyrosination. *J. Cell Biol.* **185**, 1159–1166 (2009).

26. K. I. Brackley, J. Grantham, Activities of the chaperonin containing TCP-1 (CCT): Implications for cell cycle progression and cytoskeletal organisation. *Cell Stress Chaperones* **14**, 23–31 (2009).

27. J. Otón, E. Pereiro, A. J. Pérez-Berná, L. Millach, C. O. S. Sorzano, R. Marabini, J. M. Carazo, Characterization of transfer function, resolution and depth of field of a soft X-ray microscope applied to tomography enhancement by Wiener deconvolution. *Biomed. Opt. Express* **7**, 5092–5103 (2016).

28. J. Cuéllar, W. G. Ludlam, N. C. Tensmeyer, T. Aoba, M. Dhavale, C. Santiago, M. T. Bueno-Carrasco, M. J. Mann, R. L. Plimpton, A. Makaju, S. Franklin, B. M. Willardson, J. M. Valpuesta, Structural and functional analysis of the role of the chaperonin CCT in mTOR complex assembly. *Nat. Commun.* **10**, 2865 (2019).

29. C. Betz, N. M. Hall, Where is mTOR and what is it doing there? *J. Cell Biol.* **203**, 563–574 (2013).

30. J. Busselez, F. J. Chichón, M. J. Rodríguez, A. Alpízar, S. I. Gharbi, M. Franch, R. Melero, A. Paradela, J. L. Carrascosa, J.-M. Carazo, Cryo-electron tomography and proteomics studies of centrosomes from differentiated quiescent thymocytes. *Sci. Rep.* **9**, 7187 (2019).

31. H. Soares, R. Henriques, M. Sachse, L. Ventimiglia, M. A. Alonso, C. Zimmer, M.-I. Thoulouze, A. Alcover, Regulated vesicle fusion generates signaling nanoterritories that control T cell activation at the immunological synapse. *J. Exp. Med.* **210**, 2415–2433 (2013).

32. M. Amit, S. J. Weisberg, M. Nadler-Holly, E. A. McCormack, E. Feldmesser, D. Kaganovich, K. R. Willison, A. Horovitz, Equivalent mutations in the eight subunits of the chaperonin CCT produce dramatically different cellular and gene expression phenotypes. *J. Mol. Biol.* **401**, 532–543 (2010).

33. D. Balchin, G. Miličić, M. Strauss, M. Hayer-Hartl, F. Ulrich Hartl, Pathway of actin folding directed by the eukaryotic chaperonin TRiC. *Cell* **174**, 1507–1521.e16 (2018).

34. N. Kalisman, G. F. Schröder, M. Levitt, The crystal structures of the eukaryotic chaperonin CCT reveal its functional partitioning. *Structure* **21**, 540–549 (2013).

35. S. Reissmann, L. A. Joachimiak, B. Chen, A. S. Meyer, A. Nguyen, J. Frydman, A gradient of ATP affinities generates an asymmetric power stroke driving the chaperonin TRIC/CCT folding cycle. *Cell Rep.* **2**, 866–877 (2012).

36. M. Bornens, The centrosome in cells and organisms. *Science* **335**, 422–426 (2012).

37. J. S. Andersen, C. J. Wilkinson, T. Mayor, P. Mortensen, E. A. Nigg, M. Mann, Proteomic characterization of the human centrosome by protein correlation profiling. *Nature* **426**, 570–574 (2003).

38. J. Otón, E. Pereiro, J. J. Conesa, F. J. Chichón, D. Luque, J. M. Rodríguez, A. J. Pérez-Berná, C. O. S. Sorzano, J. Klukowska, G. T. Herman, J. Vargas, R. Marabini, J. L. Carrascosa, J. M. Carazo, XTEND: Extending the depth of field in cryo soft X-ray tomography. *Sci. Rep.* **7**, 45808 (2017).

39. C. Aillaud, C. Bosc, L. Peris, A. Bosson, P. Heemeryck, J. Van Dijk, J. Le Friec, B. Boulan, F. Vossier, L. E. Sanman, S. Syed, N. Amara, Y. Couté, L. Lafanechère, E. Denarier, C. Delphin, L. Pelletier, S. Humbert, M. Bogyo, A. Andrieux, K. Rogowski, M.-J. Moutin, Vasohibins/SVBP are tubulin carboxypeptidases (TCPs) that regulate neuron differentiation. *Science* **358**, 1448–1453 (2017).

40. L. Andres-Delgado, O. M. Anton, R. Madrid, J. A. Byrne, M. A. Alonso, Formin INF2 regulates MAL-mediated transport of Lck to the plasma membrane of human T lymphocytes. *Blood* **116**, 5919–5929 (2010).

41. L. Paturle-Lafanechère, B. Manier, N. Trigault, F. Pirollet, H. Mazarguil, D. Job, Accumulation of delta 2-tubulin, a major tubulin variant that cannot be tyrosinated, in neuronal tissues and in stable microtubule assemblies. *J. Cell Sci.* **107** (Pt. 6), 1529–1543 (1994).

42. E. J. Baker, Tubulin mRNA instability and stabilization by protein synthesis inhibitors are reproducible in nontranslating extracts from *Chlamydomonas*. *Dev. Genet.* **14**, 460–470 (1993).

43. M. S. Poruchynsky, D. L. Sackett, R. W. Robey, Y. Ward, C. Annunziata, T. Fojo, Proteasome inhibitors increase tubulin polymerization and stabilization in tissue culture cells: A possible mechanism contributing to peripheral neuropathy and cellular toxicity following proteasome inhibition. *Cell Cycle* **7**, 940–949 (2008).

44. J. Oliaro, V. Van Ham, F. Sacirbegovic, A. Pasam, Z. Bomzon, K. Pham, M. J. Ludford-Menting, N. J. Waterhouse, M. Bots, E. D. Hawkins, S. V. Watt, L. A. Cluse, C. J. P. Clarke, D. J. Izon, J. T. Chang, N. Thompson, M. Gu, R. W. Johnstone, M. J. Smyth, P. O. Humbert, S. L. Reiner, S. M. Russell, Asymmetric cell division of T cells upon antigen presentation uses multiple conserved mechanisms. *J. Immunol.* **185**, 367–375 (2010).

45. A. W. Thompson, H. R. Turnquist, G. Raimondi, Immunoregulatory functions of mTOR inhibition. *Nat. Rev. Immunol.* **9**, 324–337 (2009).

46. J. Avila, H. Soares, M. L. Fanarraga, J. C. Zabala, Isolation of microtubules and microtubule proteins. *Curr. Protoc. Cell Biol.* **39**, 3.29.1–3.29.28 (2008).

47. E. Bonzon-Kulichenko, D. Pérez-Hernández, E. Núñez, P. Martínez-Acedo, P. Navarro, M. Trevisan-Herraz, M. del Carmen Ramos, S. Sierra, S. Martínez-Martínez, M. Ruiz-Meana, E. Miró-Casas, D. García-Dorado, J. M. Redondo, J. S. Burgos, J. Vázquez, A robust method for quantitative high-throughput analysis of proteomes by ^{18}O labeling. *Mol. Cell. Proteomics* **10**, M110.003335 (2011).

48. P. Navarro, M. Trevisan-Herraz, E. Bonzon-Kulichenko, E. Núñez, P. Martínez-Acedo, D. Pérez-Hernández, I. Jorge, R. Mesa, E. Calvo, M. Carrascal, M. L. Hernáez, F. García, J. A. Bárcena, K. Ashman, J. Abian, C. Gil, J. M. Redondo, J. Vázquez, General statistical framework for quantitative proteomics by stable isotope labeling. *J. Proteome Res.* **13**, 1234–1247 (2014).

49. N. Blas-Rus, E. Bustos-Morán, I. Pérez de Castro, G. de Cárcer, A. Borroto, E. Camafeita, I. Jorge, J. Vázquez, B. Alarcón, M. Malumbres, N. B. Martín-Cófreces, F. Sánchez-Madrid, Aurora A drives early signalling and vesicle dynamics during T-cell activation. *Nat. Commun.* **7**, 11389 (2016).

Citation: N. B. Martin-Cofreces, F. J. Chichon, E. Calvo, D. Torralba, E. Bustos-Moran, S. G. Dosil, A. Rojas-Gomez, E. Bonzon-Kulichenko, J. A. Lopez, J. Otón, A. Sorrentino, J. C. Zabala, I. Vernos, J. Vazquez, J. M. Valpuesta, F. Sanchez-Madrid, The chaperonin CCT controls T cell receptor–driven 3D configuration of centrioles. *Sci. Adv.* **6**, eabb7242 (2020).